Ribeiro *et al.*
Cell Communication and Signaling (2025) 23:10
https://doi.org/10.1186/s12964-024-02007-9

Cell Communication
and Signaling

RESEARCH **Open Access**

N88S seipin-related seipinopathy is a lipidopathy associated with loss of iron homeostasis

Mariana O. Ribeiro[1,2], Mafalda Oliveira[1,2], Verónica Nogueira[1,2], Vítor Costa[1,2,3] and Vitor Teixeira[1,2*]

Abstract

Background Seipin is a protein encoded by the *BSCL2* gene in humans and *SEI1* gene in yeast, forming an Endoplasmic Reticulum (ER)-bound homo-oligomer. This oligomer is crucial in targeting ER-lipid droplet (LD) contact sites, facilitating the delivery of triacylglycerol (TG) to nascent LDs. Mutations in BSCL2, particularly N88S and S90L, lead to seipinopathies, which correspond to a cohort of motor neuron diseases (MNDs) characterized by the accumulation of misfolded N88S seipin into inclusion bodies (IBs) and cellular dysfunctions.

Methods Quantitative untargeted mass spectrometric proteomic and lipidomic analyses were conducted to examine changes in protein and lipid abundance in wild-type (WT) versus N88S seipin-expressing mutant cells. Differentially expressed proteins were categorized into functional networks to highlight altered protein functions and signaling pathways. Statistical comparisons were made using unpaired Student's *t*-tests or two-way ANOVA followed by Tukey´s / Šídák's multiple comparisons tests. *P*-values < 0.05 are considered significant.

Results In a well-established yeast model of N88S seipinopathy, misfolded N88S seipin forms IBs and exhibits higher levels of ER stress, leading to decreased cell viability due to increased reactive oxygen species (ROS), oxidative damage, lipid peroxidation, and reduced antioxidant activity. Proteomic and lipidomic analyses revealed alterations in phosphatidic acid (PA) levels, associated with disrupted inositol metabolism and decreased flux towards phospholipid biosynthesis. Importantly, deregulation of lipid metabolism contributed to ER stress beyond N88S seipin misfolding and IB formation. Additionally, the model exhibited deregulated iron (Fe) homeostasis during lifespan. N88S seipin-expressing cells showed impaired ability to cope with iron deficiency. This was linked to changes in the expression of Aft1p-controlled iron regulon genes, including the mRNA-binding protein *CTH2* and the high-affinity iron transport system member *FET3*, in a p38/Hog1p- and Msn2p/Msn4p-dependent manner. Importantly, we unraveled a novel link between inositol metabolism and activation of the iron regulon in cells expressing the N88S seipin mutation. Despite iron accumulation, this was not associated with oxidative stress.

Conclusions The study highlights that the effects of N88S seipin mutation extend beyond protein misfolding, with significant disruptions in lipid metabolism and iron homeostasis. This research marks a substantial advance in understanding and defining the roles of proteins and signaling pathways that contribute to human seipinopathy. Altered cellular processes, as well as potential therapeutic targets and biomarkers, were identified and can be explored in translational studies using human cell models.

Keywords Lipid droplet, Seipin, Misfolding, Seipinopathy, Lipidopathy, Proteinopathy, Inositol, Iron

---

*Correspondence:
Vitor Teixeira
vitor.teixeira@i3s.up.pt
Full list of author information is available at the end of the article

Introduction

Lipid droplets (LDs) are ubiquitous cellular organelles responsible for fat storage, consisting of a core of triacylglycerols (TG) and sterol esters (SE) surrounded by a protein-decorated phospholipid monolayer membrane [1–3]. LD dysfunction is linked to multiple diseases, making the study of LD biogenesis pivotal for understanding basic disease mechanisms.

Seipin functions as an ER membrane protein featuring two transmembrane domains, a conserved luminal loop, and cytosolic domains that assembles into an oligomeric ring-like complex, which is essential for TG binding and proper LD budding and growth [4–9]. In several organisms, deletion of seipin leads to aberrant formation of LDs, which manifest as clustered or enlarged LDs [10–12], and impaired lipid homeostasis associated with altered cellular lipid profile and metabolic dysfunctions [13, 14]. On the other hand, gain-of-function mutations in seipin, including N88S and S90L, are associated with autosomal dominant motor neuron diseases (MNDs), such as hereditary spastic paraplegias (Silver syndrome), Charcot-Marie-Tooth disease type 2, and distal hereditary motor neuropathy type V [15–18]. The importance of seipin in nervous tissue is underscored by the observation that seipin is expressed in motor neurons in the spinal cord and cortical neurons in the frontal lobe cortex [14], consistent with degeneration of lower and upper motor neurons observed in seipinopathy [14]. In addition, it is essential for excitatory synaptic transmission and neurotransmitter release [14]. This cohort of MNDs involve gradual involvement of both upper motor neurons (resulting in gait disturbances and pyramidal signs) and lower motor neurons (leading to amyotrophy of the peroneal muscles and small hand muscles), as well as *pes cavus* [19]. The molecular mechanisms underlying seipinopathy remain largely unresolved. By disrupting *N*-glycosylation, these mutations stimulate protein aggregation, resulting in ER stress and cell death [14, 20, 21]. Expression of dominant, unglycosylated N88S and S90L variants of seipin triggers a pronounced ER stress response by activating the unfolded protein response (UPR). This activation leads to the segregation of mutant seipin into inclusion bodies (IBs). The exact composition and characteristics of these IBs are still unclear [14]. Despite these observations, the N88S seipin variant undergoes polyubiquitination and is subsequently targeted for degradation via the proteasome through the ER-associated degradation (ERAD) pathway [14, 22]. Neutral lipid metabolism, which drives LD biogenesis, is intricately linked to phospholipid biosynthesis pathways, as both processes are crucial for maintaining cellular lipid homeostasis and organellar membrane integrity [23]. The synthesis of membrane phospholipids begins with the phospholipid phosphatidic acid (PA). In the de novo pathways, membrane glycerophospholipids are synthesized from PA through the liponucleotide intermediate CDP-diacylglycerol (CDP-DAG). It can also be channelled towards the synthesis of phosphatidylglycerol (PG). Additionally, PA serves as a precursor for the synthesis of TG stored in LDs [23]. Key to this control are *cis*-acting elements like the inositol-responsive UAS_{INO}, and transcription factors including the Ino2p-Ino4p complex and the transcriptional repressor Opi1p, which orchestrate the transcriptional regulation of phospholipid biosynthetic genes [24, 25]. Genes involved in the CDP-DAG pathway (e.g., *CDS1, CHO1, PSD1, CHO2, OPI3*), and in the synthesis of phosphatidylinositol (e.g., *INO1*) are regulated by $\mathrm{UAS}_{\mathrm{INO}}$ elements in their promoters [26, 27]. This element binds the Ino2p-Ino4p heterodimer, which activates transcription when inositol levels drop. However, when Opi1p binds to Ino2p, which essentially occurs in response to an increase in inositol levels, this activation is repressed [27, 28]. It is known that Opi1p transcriptional repressor activity is influenced by its cellular localization. Although Opi1p lacks a membrane-spanning domain, it associates with the nuclear/ER membrane through interaction with the integral membrane protein Scs2p and PA via electrostatic interactions [29, 30]. When PA levels decrease (e.g., in response to an increase in inositol levels), Opi1p is no longer anchored to the ER and is translocated into the nucleus to repress transcription of *INO1* and $\mathrm{UAS}_{\mathrm{INO}}$-containing phospholipid synthesis genes [28]. Iron (Fe) is essential for various biological processes, including cell respiration, neurotransmitter synthesis, metabolism, lipid biosynthesis, and oxygen delivery [31, 32]. However, excessive iron can generate ROS, leading to the oxidation of proteins, lipids, and nucleic acids, which is harmful [33, 34]. Dysregulated iron metabolism in the brain is associated with neurological issues, promoting oxidative stress and cellular damage. Thus, cells have developed complex mechanisms to regulate iron levels [33]. In yeast, the transcription factors Aft1p and its paralog Aft2p manage the cellular response to iron deficiency by activating genes of the iron regulon [34, 35]. These factors are transported into the nucleus by karyopherin Pse1p, where they bind to target genes to initiate transcription [33, 36]. Under iron deficiency, *S. cerevisiae* activates the Fe regulon to acquire iron from the environment via reductive and non-reductive pathways [35, 36]. Iron homeostasis is also maintained by regulating iron-dependent metabolic processes. Non-essential pathways are downregulated, and iron is redirected to essential ones. Aft1p and Aft2p upregulate Cth2p, an mRNA-binding protein that restricts the expression of genes encoding iron-containing proteins or associated with iron-utilizing pathways [35, 36]. Cth2p also aids in prioritizing iron allocation towards specific pathways while stalling or inhibiting its mobilization in non-essential processes, including heme biosynthesis and mitochondrial respiration. The heme oxygenase Hmx1p degrades heme to free iron for essential pathways, helping cells survive under conditions of iron starvation [37]. Under iron-replete conditions, Aft1p is transported from the nucleus into the cytosol in a process facilitated by Msn5p. This export mechanism requires proper biosynthesis of mitochondrial Fe-S clusters and their subsequent export to the cytoplasm, ensuring inhibition of Aft1p activity when iron is readily available [38, 39]. Importantly, Aft1p phosphorylation is negatively regulated by Mitogen-Activated Protein Kinase (MAPK) Hog1p/p38 in iron-replete conditions [40], and Slt2p/Mpk1p is also involved in maintaining iron levels by directly regulating Aft1p activity [41]. Mouse models carrying human N88S seipin mutation were established [21, 42]. The animals recapitulated the neurological symptoms of human seipinopathy, displaying altered locomotor activities and gait abnormalities, as well as muscular atrophy. Axonal transport was found to be lower in these animals [42]. Neurons also showed an upregulation of the ER stress response, inasmuch as BiP, protein disulfide isomerase, and XBP1 are induced, as well as seipin aggregates [21, 42]. Activation of autophagy is also one of the many ER stress consequences, as mutant seipin aggregation is associated with the stimulation of this process [42]. We have recently developed a humanized yeast model for N88S seipinopathy. This model involves the heterologous expression of human wild-type (WT) or N88S mutant seipin in a yeast seipin null background. The human seipin is fused to either the N-terminus (VN) or the C-terminus (VC) of the Venus protein. This system successfully mimics the cellular characteristics of seipinopathy seen in mammalian models [43]. This model exhibits increased ER stress levels with aging and the formation of IBs was also observed. Notably, cells expressing N88S homo-oligomers show reduced viability, increased oxidative damage from higher generation of reactive oxygen species (ROS), lipid peroxidation, and significantly decreased antioxidant activity [43]. Using this system, we performed a multi mass spectrometry-based omics approach to investigate protein functions and delineate the signaling pathways involved in the pathological features of N88S seipinopathy. Altered cellular processes, as well as potential therapeutic targets and biomarkers, were identified and can be now explored in translational studies using human cell models.

Materials and methods

Yeast strains and plasmids

S. cerevisiae strains used in this study resulted from the W303α parental strain (RRID:NCBITaxon_4932) and are described in Table S1. Protein tagging and individual gene deletions were performed by standard PCR-based homologous recombination [44, 45]. Primers were designed using Primers-4-Yeast [46] for pFA6 and pYM plasmid sets [44, 45]. Plasmids used in this study are listed in Table S2. For cloning of *CTH2*-LacZ in the YEplac181 vector, pCM64-CTH2-FeRE-CYC1-LacZ plasmid [47] was digested with HindIII, and the insert was cloned into the HindIII restriction site of the YEplac181 vector. For cloning of ADH1pr-*CDS1*-3HA into the pRS315-UPRE-LacZ vector [43], the plasmid UG75-ADH-*CDS1*-3HA [48] was digested with SacII, and the resulting insert was cloned into the SacII restriction site of the pRS315-UPRE-LacZ vector. Plasmid YEplac181-*FET3*-LacZ was generated by digesting p*FET3*-LacZ [49] with ScaI and performing ligation into the SmaI restriction site of YEplac181. To produce plasmid YEplac181-GFP-*AFT1*, pRS426-GFP-*AFT1* [50] was cut with SacI and KpnI and the resulting insert was ligated into the same restriction sites of YEplac181. All constructs were verified either by sequencing (plasmids) or PCR (mutant strains). Strains were transformed using the standard lithium acetate procedure [51].

Culture media and growth conditions

The yeast cells were grown aerobically at 26 °C in a gyratory shaker (Elmi Sky Line Orbital Shakers) at 140 rpm using Erlenmeyer flasks. A 1:5 proportion of growth media to flask volume was used. The liquid growth media used for yeast grown were: Yeast peptone dextrose (YPD) [1% (wt/vol) yeast extract (Conda Pronadisa), 2% (wt/vol) bacto peptone (LabM) and 2% (wt/vol) glucose (Fisher Scientific)], and synthetic complete (SC) medium [2% (wt/vol) glucose (Fisher Scientific) and 0.67% (wt/vol) yeast nitrogen base (YNB) without amino acids (BD BioSciences), supplemented with appropriate amino acids and nucleotides: (0.008% (wt/vol) histidine (Sigma Aldrich), 0.008% (wt/vol) tryptophan (Sigma Aldrich), 0.04% (wt/vol) leucine (Sigma Aldrich), 0.008% (wt/vol) uracil (Sigma Aldrich) and 0.008% (wt/vol) adenine (Sigma Aldrich)]. When indicated, YNB without aa and inositol was used (FORMEDIUM, ref: CYN3701) to prepare SC-glucose medium without inositol. For solid medium, 1.5% (wt/vol) agar (Conda Pronadisa) was added, supplemented or not with 3 μM $FeSO_4$ (II).

Where indicated, myo-inositol (Sigma Aldrich) was used at a final concentration of 1 mM. The iron Fe^{2+} chelator bathophenanthrolinedisulfonate (BPS, Sigma Aldrich) was added to a final concentration of 100 μM in liquid medium to create iron-starvation conditions. Cells were grown to exponential ($OD_{600} \approx 0,6$), to the post-diauxic shift (PDS) phase (24 h after exponential phase) or to early stationary phase (48 h after exponential phase).

Proteomics analysis

For proteome analysis, cells were grown to PDS phase in SC-glucose medium. Proteomics were performed by the company BGI on a commercial basis following standard protocols [52]. The mass spectrometry proteomics data have been deposited to the ProteomeXchange Consortium via the PRIDE [53] partner repository with the dataset identifier PXD054826.

Protein preparation for proteomic analysis

Proteins were extracted with Lysis buffer (7 M urea, 2 M thiourea, 20 mM tris–HCl, pH 8.0), containing 1X Cocktail and 10 mM dithiothreitol (DTT). The samples were then sonicated on ice and centrifuged at 4 °C, 25,000 g for 15 min. The supernatant was mixed with ice-cold acetone (1:5, v/v) containing 20 mM DTT and incubated at -20 °C overnight. After centrifugation at 4 °C, 25,000 g for 15 min, the precipitate was collected, washed twice with ice-cold acetone containing 20 mM DTT, and then air-dried. To reduce disulfide bonds, the dried samples were re-dissolved in Lysis buffer (without SDS) containing 10 mM DTT (final concentration) and incubated at 56 °C for 1 h. Subsequently, 55 mM iodoacetamide (IAM, final concentration) was added to block the cysteines and the samples were further incubated for 1 h in the darkroom. Following the incubation, the samples were then precipitated with ice-cold acetone, air-dried, and finally dissolved in 0.5 M TEAB (tetraethyl ammonium bromide) (Applied Biosystems, Milan, Italy), before being used for protein quantification and subsequent iTRAQ labeling.

Peptide labeling

The protein (100 μg) was digested with Trypsin Gold (Promega, Madison, WI, USA) (30:1, protein: trypsin) at 37 °C for 16 h. Digested samples were dried by vacuum centrifugation, reconstituted in 0.5 M TEAB and processed according to the manufacturer's protocol for 6-plex iTRAQ reagent labeling (Applied Biosystems). The labeled peptide mixtures were then pooled and dried by vacuum centrifugation.

Peptide Fractionation

The Shimadzu LC-20AB liquid phase system was used, and the separation column was a 5 μm, 4.6×250 mm Gemini C18 column for liquid phase separation of the sample. The dried peptide samples were reconstituted with mobile phase A (5% acetonitrile, ACN pH 9.8), injected and eluted at a flow rate of 1mL/min using the following gradients: 5% mobile phase B (95% ACN, pH 9.8) for 10 min. 5% to 35% mobile phase B for 40 min, 35% to 95% mobile phase B for 1-min, mobile phase B for 3 min, and 5% mobile phase B for 10 min. The elution peak was monitored at a wavelength of 214 nm, and one component was collected per min. The samples were combined according to the chromatographic elution peak map to obtain 20 fractions, which were then freeze-dried.

LC–ESI–MS/MS analysis

The peptides were separated using a Thermo Easy nLC 1200 (Thermo Fisher Scientific, San Jose, CA) and loaded onto an analytical C18 column packed in-house (75 μm inner diameter, 1.8 μm column material particle size, 25 cm column length). The separation was carried out through the following effective gradient at a flow rate of 250 nL/min: 0 ~ 3 min, 5% to 10% mobile phase B (80% ACN, 0.1% FA); 3 ~ 43 min, mobile phase B increased linearly from 10 to 30%; 43 ~ 53 min, mobile phase B linearly increased from 35 to 44%; 53 ~ 63 min, mobile phase B increased from 40 to 100%; 63 ~ 70 min, 100% mobile phase B. The end of the nanoliter liquid phase separation was directly connected to the mass spectrometer.

Mass Spectrometry Detection

The eluate was subjected to nanoelectrospray ionization and entered into the tandem mass spectrometer Orbitrap Eclipse (Thermo Fisher Scientific, San Jose, CA) for DDA (Data Dependent Acquisition) mode detection. Main parameter settings: the scanning range of the primary mass spectrometer was 350 ~ 1,600m/z; the resolution was set to 60,000; the initial m/z of the secondary mass spectrometer was fixed at 100; the resolution was 15,000. The precursor ion screening conditions for secondary fragmentation were: charge 2 + to 7 +, peak intensity over 25,000, Data Dependent Mode set to Cycle Time, Time between Master Scans set to 2s. The ion fragmentation mode was HCD, the fragment ions were detected in Orbitrap, the fragmentation energy was 36, and the separation window was set to 0.7 m/z. The dynamic exclusion time was set to 45s. The AGC settings were: 1.2E6 for the first level and 5E4 for the second level.

Bioinformatics analysis

Protein identification was performed using Mascot search engine (version 2.3.02; Matrix Science, London, UK) against the *Saccharomyces* 811 (27,719 sequences) database, after removal of redundant sequences). Search parameters were set as follows: monoisotopic mass;

peptide mass tolerance at 10 ppm and fragment mass tolerance at 0.02 Da; trypsin as the enzyme; allowing one missed cleavage; + 2 and + 3 as the peptide; oxidation (M), deamidated (NQ), Itraq8plex (Y) as the potential variable modifications, and carbamidomethyl (C), iTRAQ8plex (N-term), iTRAQ8plex (K) as fixed modifications.

Protein Quantification

An automated software called IQuant [54] was used to quantitatively analyzing the labeled peptides with isobaric tags. It integrates Mascot Percolator, a well performing machine learning method for rescoring database search results, to provide reliable significant measures. To assess the confidence of peptides, the peptide-spectrum matches (PSMs) were pre-filtered at a PSM-level false discovery rate (FDR) of 1%. Then, based on the "simple principle" (The parsimony principle), identified peptide sequences were assembled into a set of confident proteins. In order to control the rate of false-positive at protein level, a protein FDR at 1%, which is based on Picked protein FDR strategy [55], was estimated after protein inference (Protein-level FDR < =0.01). The protein quantification process included the following steps: Protein identification, Tag impurity correction, Data normalization, Missing value imputation, Protein ratio calculation, Statistical analysis, Results presentation. The main IQuant quantification parameters were: Quant peptide: Use all Unique peptide; Quant number: at least one unique spectra; Normalization: VSN; Protein Ratio: Weighted average; Statistical Analysis: Permutation Test. For all the comparisons, Student's *t*-test was used to identify statistically significant changes in the proteins ($P < 0.05$), and fold changes (FCs) were calculated. For each comparison, proteins with an FC > 1.2 or < 0.83 and $p < 0.05$ were considered to be differentially expressed proteins (DEPs). In total, there were 4543 proteins identified, among which 97 and 115 were up or down regulated, respectively. Functional annotations of the proteins were conducted using Blast2GO program against the non-redundant protein database (NCBInr). The KEGG database (http://www.genome.jp/kegg/) and the COG database (http://www.ncbi.nlm.nih.gov/COG/) were used to classify and group these proteins. To identify significantly enriched GO terms and KEGG pathways, enrichment analyses will be performed based on the hyper-geometric test [56].

Lipid quantification by mass spectrometric analysis

For lipidome analysis, cells were grown to PDS phase in SC-glucose medium. Lipidomics were performed by the company BGI on a commercial basis following standard protocols. Briefly, 20 mg cells were weighed and added into 2 mL thickened centrifuge tubes. Two steel balls and 800 µL of pre-chilled dichloromethane/methanol (3:1, v/v) precipitant were added into each sample, as well as 10 µL of the prepared internal standard. Samples were subjected to an ice bath ultrasound for 10 min and refrigerated overnight at -20°C. Samples were centrifuged at 25,000 × g for 15 min at 4°C and 500 µL supernatant were taken and drained in a freezer dryer. 500 µL lipid reconstituted solution (in isopropanol: acetonitrile: water = 2:1:1) was reconstituted and shaken for 30 s. Then samples were implemented in ice bath ultrasound for 10 min and centrifuged at 25,000 × g for 15 min at 4°C. 20 µL of each sample was used and mixed as QC samples.

For UPLC-MS Analysis, waters 2777c UPLC (waters, USA) in series with Q exactive HF high resolution mass spectrometer (Thermo Fisher Scientific, USA) was used for the separation and detection of metabolites. Chromatographic separation was performed on CSH C18 column (1.7 µm, 2.1 × 100 mm, Waters, USA). In positive ion mode, solvent A was 60:40 *v*/*v* acetonitrile:water with 10 mM ammonium formate and 0.1% formic acid and solvent B was 90:10 *v*/*v* isopropanol:acetonitrile with 10 mM ammonium formate and 0.1% formic acid. In negative ion mode, solvent A was 60:40 *v*/*v* acetonitrile:water with 10 mM ammonium formate and solvent B was 90:10 *v*/*v* iso propanol:acetonitrile with 10 mM ammonium formate. The gradient conditions were as follows: 40% ~ 43% B over 0 ~ 2 min, 43% ~ 50% B over 2 ~ 2.1 min, 50% ~ 54% B over 2.1 ~ 7 min, 54% ~ 70% B over 7 ~ 7.1 min, 70% ~ 99% B over 7.1 ~ 13 min, 99% ~ 40% B over 13 ~ 13.1 min, held constant at 99% ~ 40% B over 13.1 ~ 15 min and washed with 40% B over 13.1–15 min. The flow rate was 0.4 mL/min and the injection volume was 5 µL.

The instrument Q Exactive HF (Thermo Fisher Scientific, USA) was used for LC–MS analysis. The full scan range was 70–1050 m/z with a resolution of 120,000, and the automatic gain control (AGC) target for MS acquisitions was set to 3e6 with a maximum ion injection time of 100 ms. Top 3 precursors were selected for subsequent MSMS fragmentation with a maximum ion injection time of 50 ms and resolution of 30,000, the AGC was 1e5. The stepped normalized collision energy was set to 15, 30 and 45 eV. ESI parameters were setting as: sheath gas flow rate: 40; aux gas flow rate: 10; spray voltage in positive ion mode: 3.80 V; spray voltage in negative ion mode: 3.20 V; capillary temperature: 320 °C; aux gas heater temp: 350 °C. For compound identification, full-scan and MS/MS analyses were performed using Lipidsearch v.4.1 (Thermo Fisher Scientific, USA) software. Metabolite ion peak extraction and metabolite identification for lipidomics, data preprocessing using metaX [57] and data visualization were performed as described [58]. The alteration of lipid levels was determined using the following criteria:

with a FC and Student´s *t*-test, with FC $\geq$ 1.2 or $\leq$ 0.83 and $p < 0.05$ set as the level of statistical significance.

Transcriptomics

For transcriptomics analysis, cells were grown to exponential phase in SC-glucose medium, and then BPS was added to a final concentration of 100 mM. Cells were then incubated for additional 4 h. RNA extraction, library construction, and sequencing were performed by the BGI company following internal procedures. The raw and processed RNA sequencing data are available from the NCBI GEO repository under the accession number GSE273946.

RNA extraction

Cells were homogenized by mechanical disruption in 1.5 mL TRIzol lysis buffer. Samples were centrifuged at 12,000g for 5 min in 4ºC. The supernatant was transferred to new centrifuge tubes containing a chloroform/isoamyl alcohol (24:1) mix. After each shaking step, the samples were centrifuged at 12,000g for 8 min at 4ºC. Then, the supernatant was transferred to a new centrifuge tube containing isopropyl alcohol (2/3 vol/vol), gently shaken and cooled at -20ºC. Samples were then centrifuged for 25 min at 17,500 g (4ºC) and the supernatant was transferred to new microcentrifuge tubes, and combined twice with 75% (vol/vol) ethanol and mixed by pipetting. After centrifugation at 17,500 g for 3 min (4ºC), the supernatant was discarded, and the pellet was resuspended in 20–200 μL DEPC-H_2O or RNase-free water. RNA integrity number (RIN) was used to assess the quality of the isolated RNA.

Library construction methods

mRNA enrichment was performed on total RNA using oligo(dT)-attached magnetic beads. The enriched mRNA with poly(A) tails was fragmented using a fragmentation buffer, followed by reverse transcription using random N6 primers to synthesize cDNA double strands. The synthesized double-stranded DNA was then end-repaired and 5’-phosphorylated, with a protruding ‘A’ at the 3’ end forming a blunt end, followed by ligation of a bubble-shaped adapter with a protruding ‘T’ at the 3’ end. The ligation products were PCR amplified using specific primers. The PCR products were denatured to single strands, and then single-stranded circular DNA libraries were generated using a bridged primer. The constructed libraries were quality-checked and sequenced after passing the quality control. The test methods included Agilent 2100 Bioanalyzer and ABI StepOnePlus Real-Time PCR system.

Data filtering

Sequencing was performed on a DNBSEQ platform with PE150 (read length). The sequencing data was filtered with SOAPnuke [59] by: (1) removing reads containing sequencing adapter; (2) removing reads whose low-quality base ratio (base quality less than or equal to 15) is more than 20%; (3) removing reads whose unknown base (‘N’ base) ratio is more than 5%, afterwards clean reads were obtained and stored in FASTQ format. The subsequent analysis and data mining were performed on Dr. Tom Multi-omics Data mining system (https://biosys.bgi.com).

Structure variation detection

Saccharomyces_cerevisiae_S288C_559292.NCBI.GCF_000146045.2_R64.v2201 was used a reference from NCBI. The clean reads were mapped to the reference genome using HISAT2 [60]. After that, Ericscript (v0.5.5) [61] and rMATS (V3.2.5) [62] were used to detect fusion genes and differential splicing genes (DSGs), respectively.

RNA identification

Bowtie2 [63] was applied to align the clean reads to the gene set, in which known and novel, coding and noncoding transcripts were included.

Gene quantification differential expression analysis

Expression level of gene was calculated by RSEM (v1.3.1) [64]. The heatmap was drawn by pheatmap (v1.0.8) according to the gene expression difference in different samples. Essentially, differential expression analysis was performed using the DESeq2 (v1.4.5) [65] [or DEGseq [66] or PoissonDis [67]] with *Q* value $\leq$ 0.05 (or FDR $\leq$ 0.001).

Gene annotation

To take insight to the change of phenotype, GO (http://www.geneontology.org/) and KEGG (https://www.kegg.jp/) enrichment analysis of annotated different expression gene was performed by Phyper (https://en.wikipedia.org/wiki/Hypergeometric_distribution) based on Hyper geometric test. The significant levels of terms and pathways were corrected by Q value with rigorous threshold (*Q* value $\leq$ 0.05, http://github.com/jdstorey/qvalue). Genes meeting this criterion were considered significantly enriched in the candidate gene set.

β-Galactosidase (β-Gal) activity assay

Cells harboring LacZ-reporter fusion plasmids were grown in SC-glucose medium. Cells were harvested by centrifugation, resuspended in breaking buffer (100 mM Tris, 1 mM DTT, 10% (vol/vol) glycerol) and protease inhibitors (Complete mini EDTA-free Protease cocktail inhibitor tablets, Sigma Aldrich) and mechanically lysed with zirconium beads for 5 min. Debris were pelleted at 12,044 g for 15 min at 4 ºC and the supernatant was collected for protein quantification. Total protein levels were quantified by the Lowry method using a bovine serum albumin standard curve. Volumes corresponding to 15–100 µg of total extract protein were diluted up to 800 µL with β-Gal buffer (60 mM Na_2HPO_4, 40 mM NaH_2PO_4, 10 mM KCl, 1 mM $MgSO_4$, 50 mM β-mercaptoethanol). β-Galactosidase (β-Gal) activity was measured at 30 °C using the substrate *o*-nitrophenyl-β-D-galactopyranoside (ONPG; Merck, Kenilworth, NJ, USA), as described previously [68].

Western blotting analysis

For assessment of total protein levels of Ino1p, strains WT-VN WT-VC INO1-HA and N88S-VN N88S-VC INO1-HA were grown to exponential or PDS phases in SC-glucose medium. To evaluate the phosphorylation status and total protein levels of Aft1p, strains expressing pRS415-HA-AFT1 were grown to PDS phase in SC-glucose medium at 26 ºC. The cells were washed and harvested by centrifugation for 4 min at 4000 rpm (4 ºC). Proteins were extracted by alkaline lysis, and prepared in Laemmli sample buffer. Proteins were separated by SDS-PAGE, using 10% (Ino1p-3HA/HA-Aft1p total levels) and 6% (HA-Aft1p phosphorylation) polyacrylamide gels, and transferred to nitrocellulose membranes (Hybond-ECL GE Healthcare, Cytiva) in a semi-dry system for 1 h. Membranes were blocked with 5% (wt/vol) nonfat dry milk in TTBS (20 mM Tris, 140 mM NaCl, 0.05% (vol/vol), Tween-20 pH 7.6) for 1 h. Next, membranes were incubated with primary antibodies: mouse anti-HA tag antibody F-7 (1:1000, sc-7392 Santa Cruz Biotechnology, RRID:AB_2894930) or mouse anti-Pgk1 (1:50,000, Invitrogen, RRID:AB_2532235). After washing with TTBS, membranes were incubated with the secondary antibody goat mouse IgG-peroxidase (1:5,000; Invitrogen, RRID:AB_2536527). Immunodetection was performed by chemiluminescence using WesternBright ECL reagent (Advansta) and exposing the membranes to LucentBlue X-ray films (Advansta). Band intensities were analyzed using the GS-900 Calibrated Densitometer (Bio-Rad).

Fluorescence microscopy

To examine the intracellular localization of IBs using the Venus signal upon reconstitution of the VN and VC fragments, cells were grown to exponential phase in SC-glucose medium. To evaluate the localization of GFP-Aft1p, cells transformed with YEplac181-GFP-*AFT1* were grown to the exponential phase in SC-glucose medium supplemented with 300 µM $FeSO_4$ (II). For nuclear staining, cells were incubated with 4 µg/mL of 4′-6-diamidino-2-phenylindole (DAPI, Molecular Probes, Invitrogen) for 15 min at room temperature, and protected from light. Cells were washed twice with PBS and observed by fluorescence microscopy (Zeiss Axio Imager Z1 Apotome or Leica TCS SP8). Z-stacks were acquired for DIC, DAPI and GFP/Venus channels. The output final images and colocalization analysis were performed using ImageJ 1.51k software. When applicable, all quantifications were performed from two independent experiments, and more than 100 cells per condition were scored. Colocalization between GFP-Aft1p and DAPI-marked punctae in acquired images was scored manually based on the spatial overlap between the two channels. Values were recorded in Excel (Microsoft) and analyzed in Prism 8.0 (GraphPad Software). For IB counting, budded and separate cells were used. Brightness and contrast were adjusted using Inkscape (The Inkscape Project).

Iron levels

Total iron levels were quantified in yeast cells ($3–7\times10^7$ cells mL^{-1}) grown in SC glucose medium to late exponential (OD_{600} ≈ 2) and PDS (OD_{600} ≈ 6–7.5) phases, using a colorimetric assay as described [40]. Briefly, cells were washed twice with water, resuspended in 0.5 mL of 3% (vol/vol) nitric acid, and incubated 16 h at 98°C. The supernatant (400 µL) was mixed with 160 µL of 38 mg sodium ascorbate mL^{-1}, 320 µL of 1.7 mg BPS mL^{-1} (ethanol:chloroform, 2:1), and 126 µL of ammonium acetate (saturated solution diluted 1:3). The organic phase was diluted 20-fold in ethanol:chloroform (2:1), and the absorbance was measured at 535 nm. Iron was quantified by reference to a standard curve using iron sulfate [69].

ROS staining and IB formation

To assess ROS, cells grown in SC-glucose medium at specified phases were incubated with 5 µg/mL dihydroethidium (DHE, Molecular Probes) for 10 min at room temperature in the dark. The quantification of Venus fluorescence intensity, normalized to the number of cells, was used as a means to monitor IB formation [43]. Then, cells were centrifuged, washed twice and resuspended in PBS [43]. Flow cytometry analysis was performed using the FL1 (533/30) for IB monitoring, and FL3 (670 LP) channels (BD Accuri C6 Flow cytometer) for ROS quantification via DHE. Data were evaluated with FlowJow software (v. 10.6.1).

Yeast spotting assay

The oxidative stress agents *tert*-Butyl hydroperoxide (*t*-BOOH, Sigma Aldrich) and hydrogen peroxide (H_2O_2, Merck) were added at a final concentration of 50 µM and 250 µM to iron-supplemented SC-glucose plates. The iron chelator BPS was added to a final concentration of 30 µM. Growth assays were performed by spotting 1:10 serial dilutions of exponentially grown cell cultures onto SC-glucose plates and containing the specified compounds. The growth was observed and recorded after a 2-day incubation period at 26°C.

Bioinformatics analysis

In-silico analysis of transcriptional regulation of the *FET3* promoter was carried out using the Yeast Search for Transcriptional Regulators and Consensus Tracking (YEASTRACT+) database [70]. The search was performed to define unbiased regulatory associations between transcription factors (TFs) and the promoter region, either document or potential associations (based on TF binding sites). YEASTRACT+was also used to find genes encoding proteins found to be elevated in the mutant strain and regulated by Msn2/Msn4p. For that, documented associations between genes and transcription factors Msn2p and Msn4p were searched using the following parameters: 1) Simultaneous DNA binding and expression evidence and 2) Transcription factor acting as activator.

Aconitase activity assay

The measurement of aconitase activity was performed as described [49, 71, 72], with minor modifications. Briefly, cells were grown to PDS phase in SC-glucose medium and harvested by centrifugation for 5 min at 4000 rpm (4 ºC). Cells were resuspended in aconitase buffer (100 mM Tris–HCl pH 7.4 and 0.6 M sorbitol) containing protease inhibitors (Complete mini EDTA-free Protease cocktail inhibitor tablets, Sigma Aldrich). The protein extracts were obtained by vortexing in the presence of glass beads for 10 min. Cell debris was removed by centrifugation at 3000 rpm for 15 min at 4 ºC, and protein concentration was determined by the method of Lowry, using bovine serum albumin (Sigma Aldrich) as a standard. Cell lysates were assayed at 25 °C in aconitase reaction buffer containing 100 mM Tris–HCl (pH 7.4), 1.2 mM *cis*-aconitate (Sigma-Aldrich) and 45 µL of protein sample. The lysis and enzymatic activity measurement steps were performed under an anaerobic atmosphere using buffers flushed with nitrogen gas. The decrease in absorbance at 240 nm was measured as a function of time (normalized to protein concentration), and an extinction coefficient of 3.6 $(\text{mM.cm})^{-1}$ was used to calculate the specific activity of aconitase. 1 unit of aconitase activity is defined as 1 nmol of *cis*-aconitate converted per minute and per mg of protein.

Statistical analysis

Unless specified otherwise, the results were derived from a minimum of three independent experiments. The images shown are representative of these findings. Quantitative data are presented as the mean ± standard deviation (SD). Statistical comparisons were made using unpaired, two-tailed Student's t-tests or two-way ANOVA, conducted with Prism 8.0 software (GraphPad Software). P-values < 0.05 were considered significant: $^{*}p \leq 0.05$; $^{**}p \leq 0.01$; $^{***}p \leq 0.001$; $^{****}p \leq 0.0001$.

Results

Lipid metabolism is altered in N88S seipin-expressing cells

In this study, we employed comparative unbiased quantitative mass spectrometric proteomic analysis to examine changes in protein abundance and profile between the WT-VN WT-VC and N88S-VN N88S-VC strain at the post-diauxic shift (PDS) phase, when cells shifted from a fermentative (exponential phase) to aerobic utilization of non-glycolytic substrates (e.g. ethanol) by mitochondria. The goal was to define a set of differentially expressed proteins (DEPs—either up- or down-regulated) and sort into functional networks to highlight perturbed protein functions and signalling pathways contributing to disease-related phenotypes. We were able to identify 115 proteins with reduced abundance and 97 proteins with increased abundance in N88S seipin-expressing cells (Fig. 1A and Fig. S1A, Tables S3 and S4).

(See figure on next page.)

Fig. 1 Proteomic analysis of WT and N88S seipin-expressing cells. **A** Number of proteins significantly up- or down-regulated in the mutant strain. **B** The volcano plot illustrates the differentially expressed proteins (DEPs) in the N88S seipin mutant compared to the WT strain. The x-axis represents the log2 fold-change, while the y-axis shows the -$\log_{10}$ P-value, indicating the probability of differential expression. A P-value < 0.05 and a fold-change > 1.2 were used as the significance thresholds for differential expression. Points of interest, marked in red and blue, highlight proteins with both substantial fold-change and high statistical significance. Red dots and blue dots indicate significantly up-regulated and down-regulated proteins, respectively. Grey dots correspond to proteins that were not significantly differentially expressed. **C** Gene Ontology (GO) term enrichment analysis on biological processes was conducted for proteins exhibiting statistically significant alterations in N88S seipin-expressing cell samples. **D** Heat map analyses of total protein level changes of enzymes of the phospholipid biosynthesis pathway in WT and N88S seipin-expressing cells (for the 3 independent experiments for each strain)

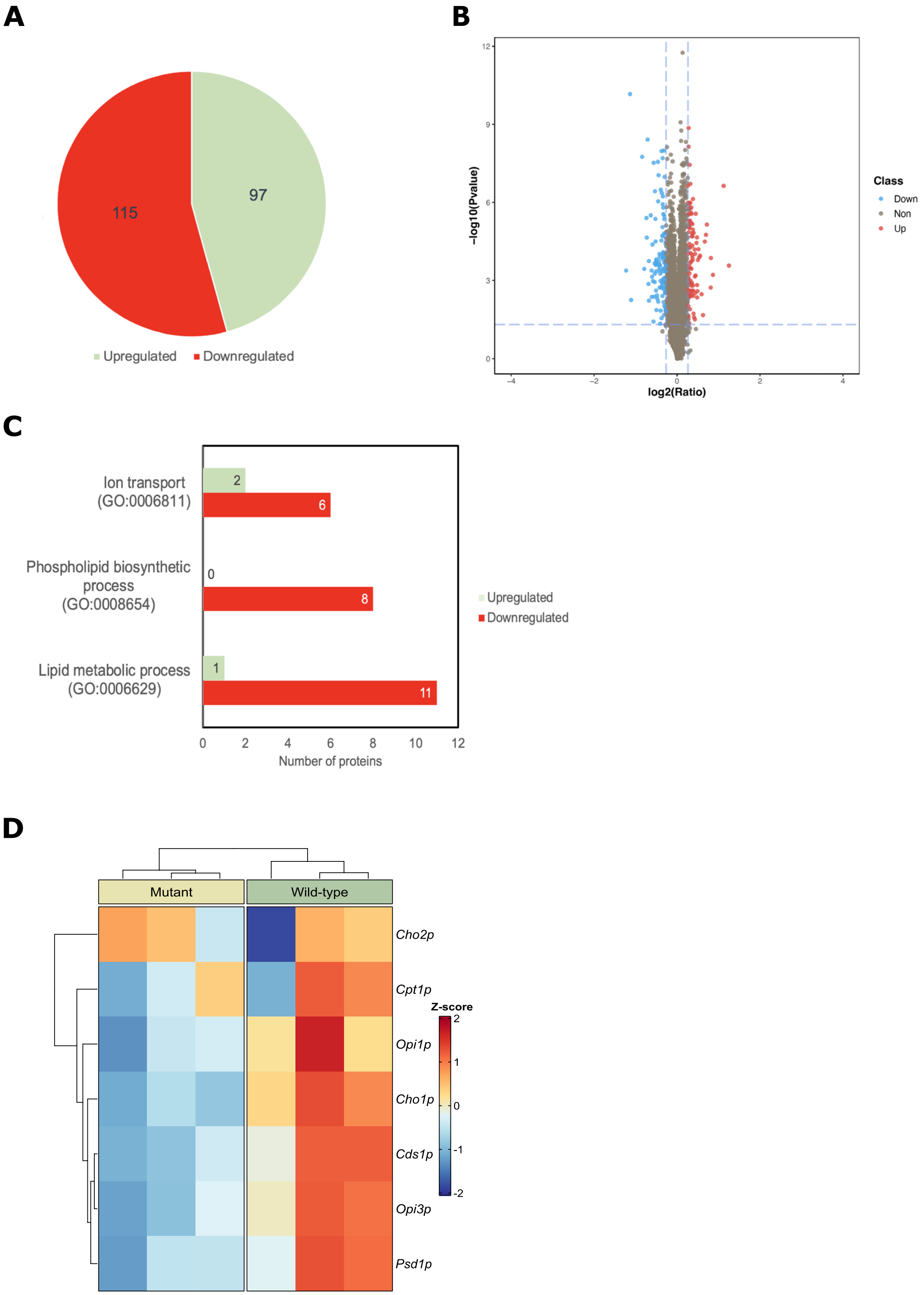

Fig. 1 (See legend on previous page.)

A volcano plot (Fig. 1B) is shown to highlight the differences in protein levels. Using YEASTRACT + [73], a Gene Ontology (GO) analysis and KEGG pathway analysis for DEPs in biological processes revealed an enrichment in proteins related to ion transport (GO:0006811; p-value = 0.001380), phospholipid biosynthetic process (GO:0008654; p-value = 2.920×10^{-9}) and lipid metabolic process (GO:0006629; p-value = 1.562×10^{-6}) (Fig. S1B-C and Fig. 1C).

Notably, among the protein identified, seven showed reduced abundance, including seven key players in the phospholipid biosynthetic pathway: Cho1p, Cho2p, Opi1p, Opi3p, Psd1p, Cpt1p and Cds1p (Table S3 and Fig. 1D). This suggests potential alterations in the lipid profile, particularly in phospholipid content. To investigate these changes, we conducted a quantitative lipidomic analysis at the same growth phase (PDS phase) to measure the levels of major phospholipids and their derivatives, inositol phosphates, and neutral lipids along with their corresponding precursors (Table S5). We observed a decrease in 46 lipid metabolites, while 41 lipid molecules levels were increased (Fig. S2A-B). The levels of fatty acids and ceramide (Fig. S2C and S2D) and of major phospholipids (PC, PE, PG, PS and PI) remained essentially unaltered (Fig. 2A). The amount of lysophospholipids (Fig. 2B) was increased, suggesting that the activity of lysophospholipid acyltransferases may be impaired in the mutant. Despite the fact of DG and TG abundance was unchanged (Fig. 2C and 2D), the levels of PA are increased (Fig. 2E).

Inositol metabolism is deregulated in cells expressing the mutant seipin

Genes encoding enzymes in both the CDP-DAG (*CDS1, CHO1, PSD1, CHO2, OPI3*) and Kennedy (*CPT1*) pathways contain a $\mathrm{UAS_{INO}}$ element in their promoters whose expression is transcriptionally repressed by Opi1p [28, 74]. To evaluate if their lower protein abundance in N88S seipin-expressing cells correlates with reduced transcription, we measured the transcription of Opi1p-dependent genes in WT and mutant cells, using an *INO1*-LacZ transcriptional reporter during lifespan. We observed that *INO1* expression remains unchanged in the WT, however there is a ~ fourfold increase in N88S seipin-expressing cells at PDS and stationary phases (Fig. 3A). It was previously demonstrated that the accumulation of PA acts as the metabolic signal that triggers the derepression of *INO1* [26, 75, 76]. Therefore, a plausible explanation for lower Opi1p repressor activity is the retention of Opi1p in the ER potentiated by accumulation of PA as observed by lipidomic analysis (Fig. 2D), allowing the Ino2p-Ino4p heteromeric complex to stimulate the transcription of *INO1*. We then conclude that post-transcriptional mechanisms may operate to control the steady protein levels of these phospholipid biosynthetic enzymes in response to changes in the lipid profile observed in the mutant strain (Fig. 1D). More recently, it was shown that the levels of PA (34:1) is correlated with optimal expression of *INO1* irrespective of total PA content [77]. We observed that the amount of the PA (34:1) is increased by ~ sevenfold at PDS phase in mutant cells, which coincides with the increase in *INO1* expression at the same phase (Fig. S2E).

Next, we decided to evaluate if higher *INO1* expression was correlated with changes in Ino1p protein levels during lifespan. For that, we analyzed Ino1p-HA levels at the exponential and PDS phases by Western Blotting. We observed increased protein levels starting at the exponential phase, which remained elevated during the PDS phase (Fig. 3B), where *INO1* expression is largely derepressed in mutant cells (Fig. 3A). Ino1p is essential for the de novo biosynthesis of inositol, which is incorporated into phosphatidylinositol (PI) for the synthesis of phosphatidylinositol phosphates (PIP). In N88S seipin-expressing cells, we also observed changes in PI-derived lipids, including decreased levels of phosphoinositides (PIP and $\mathrm{PIP_3}$). This indicates that PI metabolism is also deregulated (Fig. S2F).

We next tested whether cells expressing the seipin N88S mutation are responsive to changes in inositol levels. For that, cells expressing the *INO1*-LacZ reporter fusion were grown to exponential phase in the absence of inositol and then shifted to medium containing inositol. While WT cells adapted to inositol by reducing *INO1* expression, the mutant was unable to adapt and failed to repress *INO1* expression (Fig. 3C). Importantly, in the absence of inositol, *INO1* expression was lower in the mutant compared to WT cells which is reminiscent of the behavior displayed by the mutant $\mathrm{Opi1^{FFAT}}$, in which the Opi1p-Scs2p interaction motif two phenylalanines (FF) in an acidic tract (FFAT) is absent, and the activity of Opi1p is mainly driven by the electrostatic interaction with PA is absent, and the activity of Opi1p is mainly driven by the electrostatic interaction with PA [78]. Overall, we provide strong evidence that inositol and lipid metabolism is highly deregulated in the mutant.

In summary, the results suggest that increased PA levels may be linked to decreased flux of lipid precursors into phospholipid biosynthesis, due to lower protein levels of key enzymes in this pathway. Consequently, accumulation of PA levels likely causes Opi1p to be retained in the ER, allowing the transcription of *INO1* to be derepressed, thus leading to elevated Ino1p protein levels.

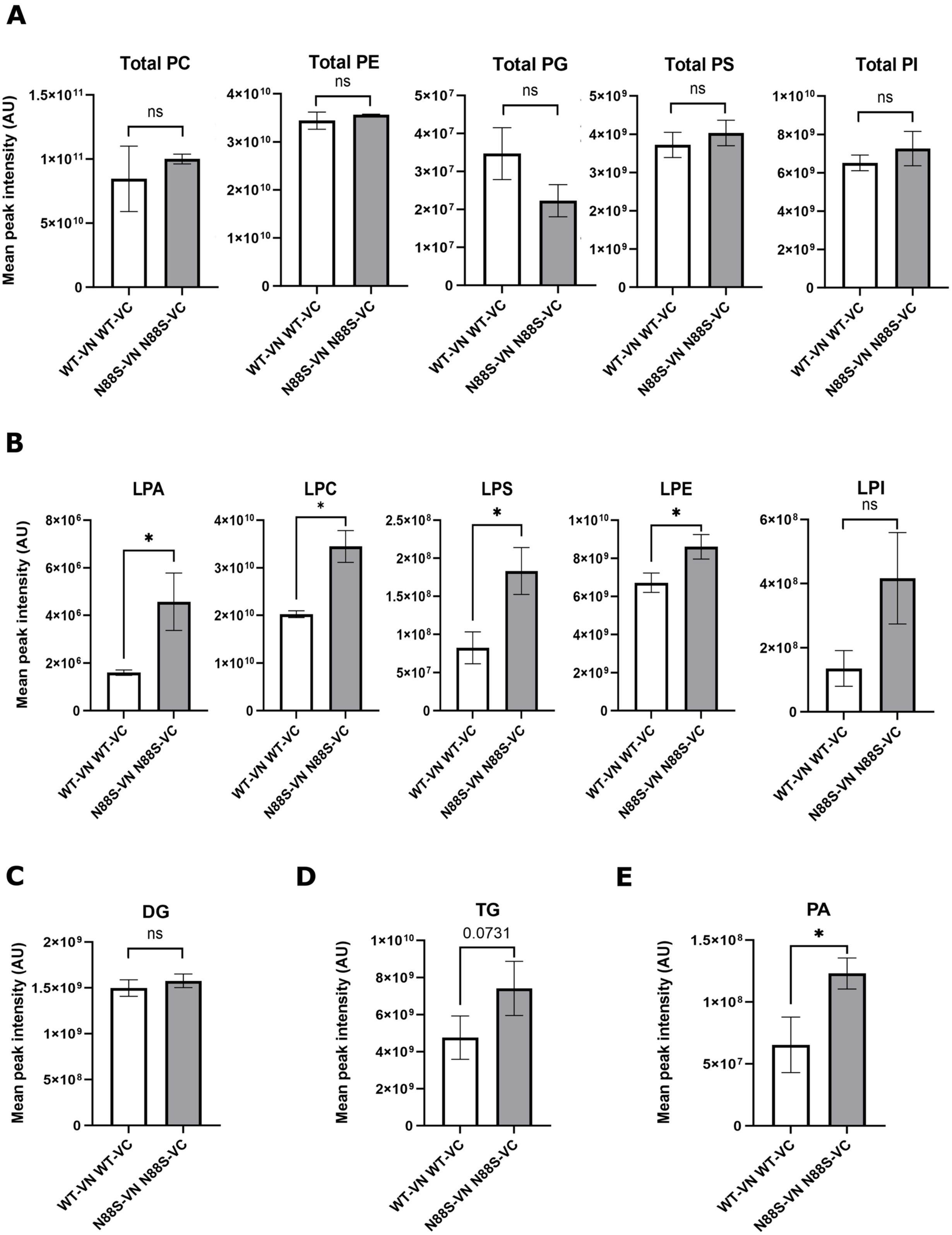

Fig. 2 Lipidomic analysis of WT and N88S seipin-expressing cells. Total levels of phospholipids (**A**), lysophospholipids (**B**), diacylglycerol/DG (**C**), phosphatidic acid/PA (**D**) and triacylglycerols/TG (E) in the N88S seipin mutant compared to WT cells grown to post-diauxic shift (PDS) phase in SC-glucose medium. Results are mean ± SD ($n = 3$). *$p \leq 0.05$ (unpaired *t*-test with Welch´s correction)

PA and impaired inositol metabolism contribute to ER stress independently of protein misfolding in mutant cells

ER stress and UPR activation can influence cellular processes beyond ER protein folding, playing critical roles in lipid metabolism, as it constitutes a key site for lipid synthesis and storage [79]. Previous studies showed that inositol depletion can trigger ER stress without causing a noticeable accumulation of unfolded proteins in the ER lumen [80–82]. Instead, this stress response appears to activate the UPR via a membrane-based mechanism that functions independently of unfolded proteins [83]. This offers an ideal framework to investigate whether deregulated lipid metabolism contributes to ER stress observed in the yeast model of N88S seipinopathy. We then evaluated how *INO1* deficiency affects the activity of the UPRE-LacZ ER stress reporter. As previously described, N88S seipin-expressing cells displayed higher levels of ER stress (Fig. 3D) associated with elevated expression of the reporter fusion [43]. Importantly, β-galactosidase activity further increased in mutant cells upon deletion of *INO1*, although to lower extent, indicating that misregulation of *INO1* expression and impaired inositol metabolism also contribute to ER stress.

Notably, *INO1* deletion is associated with reduced PI levels and accumulation of lipid precursors, including PA and CDP-DAG [28]. This led us to investigate whether accumulation of PA is associated with higher induction of the UPR. When WT cells are grown in inositol-depleted conditions, PI levels remain low, leading to PA buildup [28]. Importantly, under these conditions, N88S seipin-expressing cells exhibited higher UPR levels when grown in the absence of inositol in a *INO1*-dependent manner (Fig. 3E). In the presence of exogenous inositol, where PA is consumed as a precursor to support PI biosynthesis, the β-galactosidase activity of the ER stress reporter remained unchanged in WT cells regardless of inositol levels, but decreased in the mutant (Fig. 3E). This reinforces the hypothesis that the response to changing PA levels involves the induction of the UPR in cells expressing N88S mutant seipin.

Next, we tested how the overexpression of *CDS1* affects the ER stress response. Cds1p is responsible for the synthesis of CDP-DAG from PA. Cds1p consumes the PA pools and channels the CDP-DAG pool towards PI biosynthesis under conditions of inositol surplus [84]. However, in the absence of inositol, where PI biosynthesis is essentially halted, CDP-DAG derived from PA is channeled into the phospholipid biosynthetic pathway. Under inositol starvation, we observed that the UPR is significantly increased in WT cells, and even more induced in N88S seipin-expressing cells upon overexpression of *CDS1* (Fig. 4A). Higher UPR induction in the mutant might be linked to reduced enzymatic capacity to promote phospholipid biosynthesis under these conditions, as the overall phospholipid biosynthesis rate is likely reduced due to decreased protein levels of key enzymes involved in the pathway (Fig. 1D). So, we tested whether stimulation of phospholipid biosynthesis by overexpressing *CHO1* in WT and N88S mutant cells induces ER stress under the same conditions (in the absence of inositol). In this case, we observed no changes in the induction of the LacZ reporter fusion for all strains tested (Fig. 4B). Notably, overexpression of *CDS1*, in contrast with *CHO1* counterparts, leads to inositol auxotrophy and significant viability loss in the absence of inositol (Fig. 4C). Overall, the data support a model in which the accumulation of PA, whether due to a reduced rate of phospholipid biosynthesis or in response to changes in lipid flux upon inositol availability (Fig. 1D, 3C-E, and 4A-B), is a key feature of the ER stress response in N88S seipin mutant cells. This is particularly significant, as it demonstrates that lipid imbalance also contributes to the ER stress

(See figure on next page.)

Fig. 3 Inositol and phospholipid metabolism is impaired and contributes to the ER stress response in N88S seipin-expressing cells. **A** Opi1p-controlled expression of *INO1* promoter is increased in N88S-seipin expressing cells during lifespan. Cells of specified genotypes expressing *INO1*-LacZ were grown in SC-glucose medium and allowed to reach exponential (EXP), post-diauxic shift (PDS) and stationary (STAT) phases. Specific β-galactosidase (β-Gal) activity was measured as described Material and Methods. Left side: comparison between phases within the same strain. Right side: comparison between phases (WT vs N88S). Two-way ANOVA followed by Tukey's multiple comparison test was used; $n = 3$. **B** Western blot showing total Ino1p-HA protein levels at the indicated periods of growth. Pgk1p was used as loading control. WT (WT-VN WT-VC INO1-HA) and N88S seipin-expressing cells (N88S-VN N88S-VC INO1-HA) were grown in SC-glucose medium during growth and aliquots were collected at different stages as indicated. **C** Overnight precultures of cells expressing *INO1*-LacZ grown in SC-glucose medium lacking inositol were diluted to $OD_{600} = 0.2$ and resuspended in fresh SC medium supplemented (or not) with inositol (1 mM) and incubated for 4 h. β-galactosidase activity was measured as in Fig. 3A. Unpaired *t*-test with Welch´s correction was used; $n \geq 3$. **D** Cells of specified genotypes expressing *UPRE-LacZ* were grown in SC medium and allowed to reach the exponential phase. Specific β-galactosidase (β-Gal) activity was determined as in Fig. 3A. Unpaired *t*-test with Welch´s correction was used; $n \geq 4$. **E** Overnight precultures of cells expressing *UPRE-LacZ* grown in SC-glucose medium lacking inositol were diluted to $OD_{600} = 0.2$, resuspended in fresh SC medium lacking inositol and incubated for 4 h. Half of the culture was collected by centrifugation, while the remaining culture was incubated in SC-glucose medium supplemented with inositol (1 mM) for 2 h. Specific β-galactosidase (β-Gal) activity was assessed as in Fig. 3A. Unpaired *t*-test with Welch´s correction was used; $n \geq 4$. Results are mean ± SD. * $p \leq 0.05$; ** $p \leq 0.01$; *** $p \leq 0.001$; **** $p \leq 0.0001$; ns—non-significant

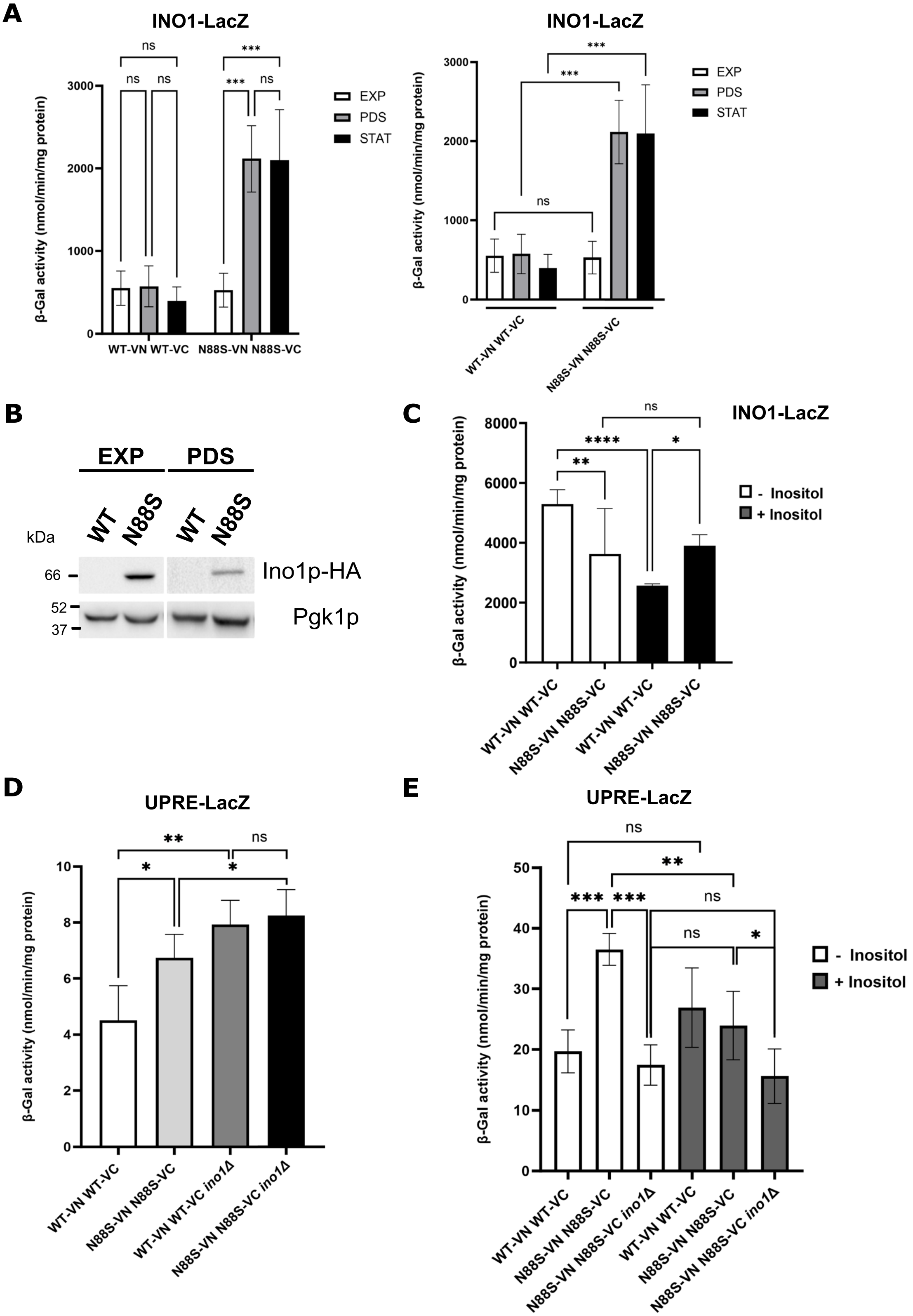

Fig. 3 (See legend on previous page.)

response beyond protein misfolding of seipin caused by the N88S mutation. In agreement with this idea, we found that *INO1* deletion actually reduced IB formation by ~ 50% in N88S seipin-expressing cells, as monitored by fluorescence microscopy and flow cytometry (Fig. 4D-E), despite the earlier observation that the UPR is more strongly induced in cells grown under the same conditions (Fig. 3D). Interestingly, while *SEI1* deletion reportedly has no significant impact on the UPR [85], the N88S mutation activates the ER stress response. Our findings link this activation to altered inositol metabolism, highlighting a unique characteristic of the N88S mutation compared to seipin mutant cells. Finally, we tested the relationship between impaired lipid metabolism and ROS production in the mutant strain. For this purpose, cells were grown to stationary phase, and ROS levels were detected using the DHE probe. The results showed that *INO1* deficiency reduced ROS levels by ~ 30% in WT cells, but did not affect ROS levels in mutant cells (Fig. S3A). This indicates that oxidative damage is not directly linked to defects in membrane lipid metabolism in N88S seipin-expressing cells.

N88S seipin expressing cells are sensitive to iron deficiency conditions

Proteomics analysis reveals changes in iron homeostasis in N88S mutant cells

The proteomic analysis revealed that proteins involved in iron ion homeostasis, including Fit1p, Arn1p, Arn2p and Hmx1p, were present at lower levels in N88S seipin expressing cells (Fig. 1C and Table S3). This prompted us to investigate whether there were alterations in cellular iron levels during lifespan imparted by the N88S seipin mutation. The results revealed that cells expressing the N88S seipin mutant accumulated iron (Fe) at the exponential phase (Fig. 5A). Nevertheless, there was a significant decrease in Fe levels from the exponential to PDS phase in the mutant, contrarily to WT cells, which were able to maintain similar Fe levels. It is known that the demand for iron increases during the diauxic shift, and Aft1p is responsible for the regulation of proteins involved in capturing, internalizing, and mobilizing Fe to meet the needs of mitochondria, DNA repair, and other cellular processes [86–88]. Using a LacZ reporter where the Aft1p binding sequence from the *CTH2* promoter is fused to the LacZ gene, we found that Aft1p transcriptional activity boosted ~ 15-fold in WT cells grown from exponential phase to PDS phase. In contrast, in N88S seipin-expressing cells, the increase was approximately sevenfold, about half of the one observed in WT cells (Fig. 5B). This is in agreement with decreased protein levels of Fit1p, Arn1p, Arn2p and Hmx1p observed in these cells at PDS phase as identified by proteomic analysis (Table S3), which collectively correspond to proteins whose genes are transcriptionally activated by Aft1p/Aft2p in response to iron deficiency [34]. To test if this effect is related to impaired ability to activate the iron regulon, cells were grown to the exponential phase and treated with the iron chelator bathophenanthrolinedisulfonate (BPS), which limits iron availability and causes an iron deprivation condition. As expected, β-galactosidase activity was significantly increased in WT cells as an adaptive response to BPS-induced iron depletion, but the reporter activity was lowered by 50–60% in the mutant strain compared to WT cells (Fig. 5C).

Transcriptomic analysis reveals significant changes in gene expression in response to iron deficiency in N88S mutant cells

To further address how Aft1p deregulation affects the iron deficiency response in cells expressing mutant seipin, WT and N88S seipin-expressing cells were subjected to transcriptomic analysis under BPS-induced iron deprivation (Fig. S4A-D). As expected, bioinformatic analysis revealed that GO functional categories were enriched among differentially expressed genes (DEGs) involved in iron-regulated processes and mitochondrial-related functions, namely tricarboxylic acid cycle and mitochondrial electron transport chain, iron-sulfur cluster assembly, sterol biosynthetic process and aminoacid metabolism (Fig. S4A-D). The results revealed

(See figure on next page.)

Fig. 4 Dysregulation of inositol and phospholipid biosynthetic pathways leads to ER stress and IB formation in cells with the N88S seipin mutation. **A**-**B** Cells with the indicating genotypes expressing *UPRE-LacZ* were precultured overnight in SC-glucose medium. Cells were centrifuged, washed twice with water, diluted to $OD_{600} = 0.2$ and resuspended in fresh SC medium lacking inositol and incubated for 4 h. Specific β-galactosidase (β-Gal) activity was assessed as in Fig. 3A. Unpaired *t*-test with Welch´s correction was used; $n \geq 4$. **C** Cells of specified genotypes expressing *UPRE-LacZ* were grown as in Fig. 4A. Tenfold dilution series were spotted onto SC-glucose plates lacking inositol, or supplemented with inositol (1 mM) when indicated. Plates were incubated at 26°C for 2 days. **D** Formation of IBs was monitored by fluorescence microscopy using the YFP/Venus channel (left panel) in cells grown to the exponential phase in SC-glucose medium. Quantification is defined as percentage of cells displaying IB foci ($n > 100$ cells, right panel). Data were combined from 2 independent experiments. DIC: Differential interference contrast. Bar scale, 8 µm. **E** Formation of IBs was monitored by flow cytometry using the FL1 channel and quantification of the Venus fluorescence intensity, normalized to cell number, was determined in cells grown to stationary phase. Unpaired *t*-test with Welch´s correction was used; $n = 3$. Results are mean ± SD. * $p \leq 0.05$; ** $p \leq 0.01$; **** $p \leq 0.0001$; ns—non-significant

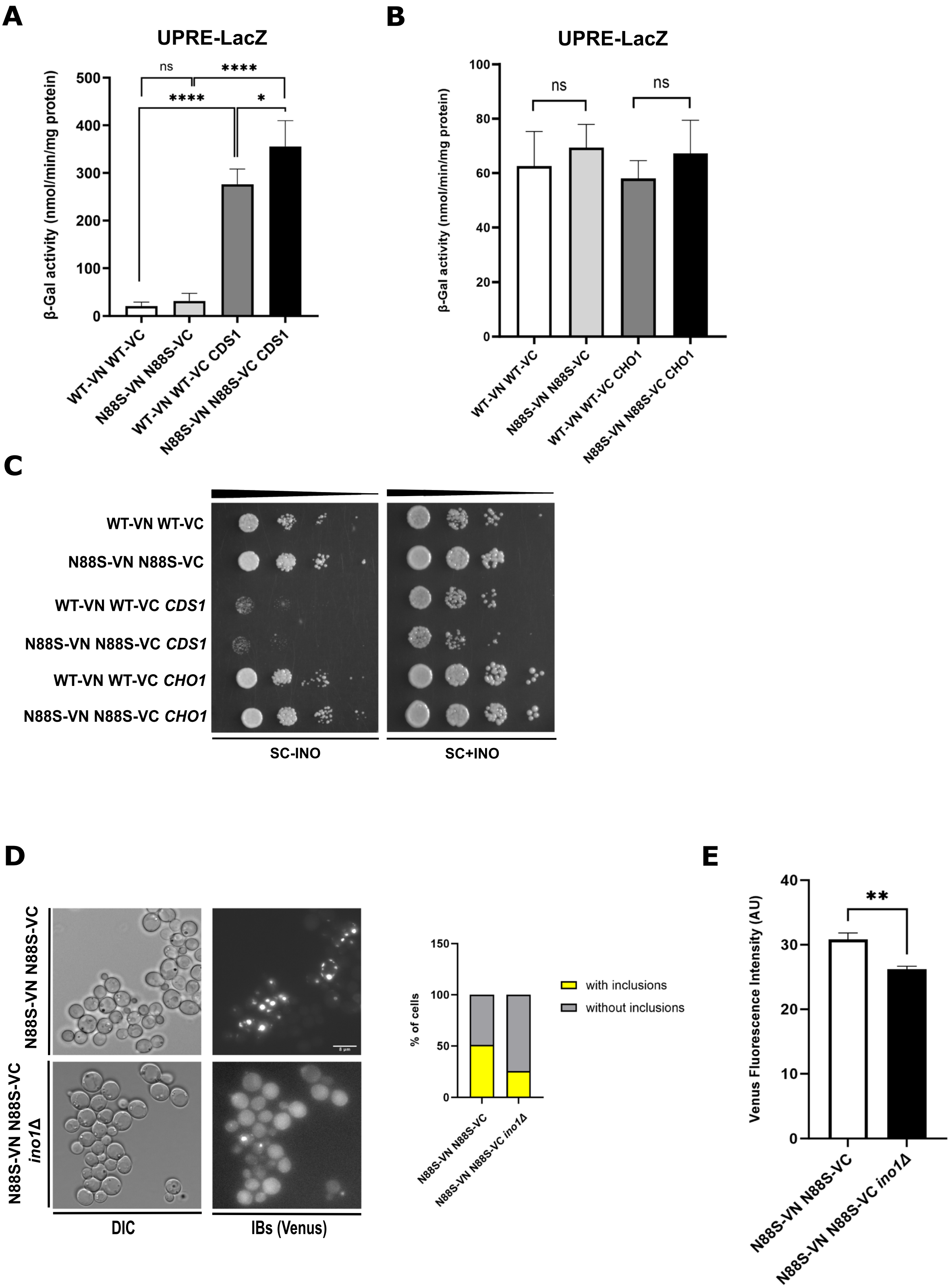

Fig. 4 (See legend on previous page.)

that 197 and 250 genes had lower and higher expression in the mutant respectively, when compared to WT cells (Tables S6 and S7). We thus focused our attention on transcripts that are transcriptionally regulated by Aft1p/Aft2p upon BPS treatment, as defined in a previous study [47]. Of the DEGs, 10 out of 28 genes previously reported to be upregulated during Fe starvation in WT cells [47] are downregulated in N88S seipin-expressing cells, including members of the Fe regulon: *CCC2, ARN1, FIT1, FTH1, OLE1, FIT3, FET4, ATX1, SIT1* and *FTR1* (Fig. S4E and Table S7). Conversely, 13 (*ISA1, COR1, PYC2, LEU1, RNR4, BIO2, CYC1, HAP4, NFU1, CCP1, CYT1, QCR2 and RIP1*) out of 34 genes with reduced expression in WT cells under similar conditions [47] are increased in the mutant strain (Fig. S4E and Table S6).

Overall, these results suggest that the N88S mutation renders cells unable to effectively activate Aft1p-mediated transcription of the iron regulon in response to changes in iron levels during lifespan and in response to iron deficiency. We then propose that this defective response may contribute to the increased ROS generation and oxidative damage previously reported for the mutant strain [43]. To test this, cells were incubated with BPS at different growth phases and then allowed to grow in medium for 48 h. When treated with the iron chelator at the exponential phase, where iron accumulation was observed in mutant cells (Fig. 5A), both WT and N88S seipin-expressing cells exhibited an acute growth defect (Fig. 5D). Although an increase in ROS content was noted in BPS-treated WT cells, the mutant displayed similar levels of ROS regardless of the presence of BPS in the medium (Fig. 5D). When cells were incubated with BPS at the diauxic shift, we observed no changes in growth and ROS content in WT and mutant cells (Fig. 5E). Altogether, the results suggest that disruption of iron homeostasis is not the primary cause of oxidative damage in the yeast model of N88S seipinopathy.

The MAPK Hog1p/p38 contributes to impaired iron metabolism in cells carrying the seipin N88S mutation

Hog1p activation and Aft1p phosphorylation and localization in N88S seipin mutant cells

The regulation of Aft1p phosphorylation by the MAPK kinases Hog1p and Slt2p has been implicated in the control of iron homeostasis [40, 41]. In particular, Hog1p negatively regulates Aft1p transcriptional activity, which allows its export from the nucleus to the cytosol under iron sufficient conditions [34, 35, 40, 89]. Based on this, we posit that reduced activation of the iron regulation by Aft1p might be associated with changes in Hog1p activation and/or Aft1p phosphorylation. Detailed proteomic analysis revealed increased levels of Sko1p (Table S4). Sko1p is a key transcription factor regulating osmostress-induced and cAMP-responsive element (CRE) gene expression under the direct control of the Hog1p [90]. The expression analysis of CRE-driven reporter genes depends solely on Sko1p-Hog1p signaling [91–93]. Using a 2xCRE-LacZ reporter, we evaluated changes in Hog1p activation during lifespan. At the exponential phase, we observed no significant changes, however a higher activation of the reporter fusion was observed in N88S seipin-expressing cells at PDS phase, indicating higher Hog1p activation (Fig. 6A). This coincided with reduced Aft1p transcriptional activity at this phase (Fig. 5B). To evaluate changes in Aft1p phosphorylation, we analyzed the migration pattern of HA-tagged Aft1p using Western blotting at PDS phase (Fig. 6B). Although total Aft1p levels are slightly higher (but not statistically significant), no noticeable alterations in the phosphorylation mobility pattern of Aft1p were observed in the mutant compared to WT cells (Fig. 6B). As a result, we conclude that the Aft1p phosphorylation status is not a primary cause for defective activation of the iron regulon at PDS phase (Fig. 5B).

We next investigated the localization of GFP-Aft1p in WT and mutant cells using fluorescence microscopy.

(See figure on next page.)

Fig. 5 Aft1p-mediated transcriptional activity is diminished at the diauxic shift and under iron-depleted conditions in cells expressing the N88S seipin mutation. **A** Total iron levels were quantified in WT and N88S seipin-carrying cells grown to exponential (EXP) and post-diauxic shift (PDS) phases. Two-way ANOVA followed by Šídák's multiple comparison test was used; $n = 4$. **B** Cells with the indicated genotypes expressing YEplac181-*CTH2*-LacZ were grown in SC-glucose medium and allowed to grow to the indicated phases. Specific β-galactosidase (β-Gal) activities were determined as in Fig. 3A. Two-way ANOVA followed by Šídák's multiple comparison test was used; $n \geq 4$. **(C)** Cells carrying YEplac181-*CTH2*-LacZ were grown to the exponential phase and treated or not with bathophenanthrolinedisulfonate (BPS, 100 µM) for 4 h. When indicated, the medium also contained $FeSO_4$ (II) at a final concentration of 5 mM, in order to repress the iron regulon. Specific β-galactosidase (β-Gal) activities were measured as in Fig. 3A. Two-way ANOVA followed by Šídák's multiple comparison test was used; $n \geq 3$. **D** Overnight precultures of cells grown in SC-glucose medium were diluted to $OD_{600} = 0.15$ in fresh medium. BPS was added at a final concentration of 100 µM and cells were allowed to grow for 48 h. The growth rate was monitored by optical density (OD) at 600 nm ($OD_{600,}$ left panel). ROS levels were assessed with the same cells labeled with dihydroethidium (DHE) via flow cytometry using the FL3 channel (right panel). Unpaired *t*-test with Welch´s correction was used; $n = 4$. **E** Cells were grown as in Fig. 5D, except that BPS was added only 24 h (at PDS phase) after the dilution step. The growth rate and ROS levels were determined accordingly after a 24 h incubation period. Unpaired *t*-test with Welch´s correction was used; $n \geq 3$. Results are mean ± SD. ** $p \leq 0.01$; *** $p \leq 0.001$; **** $p \leq 0.0001$; ns-non-significant

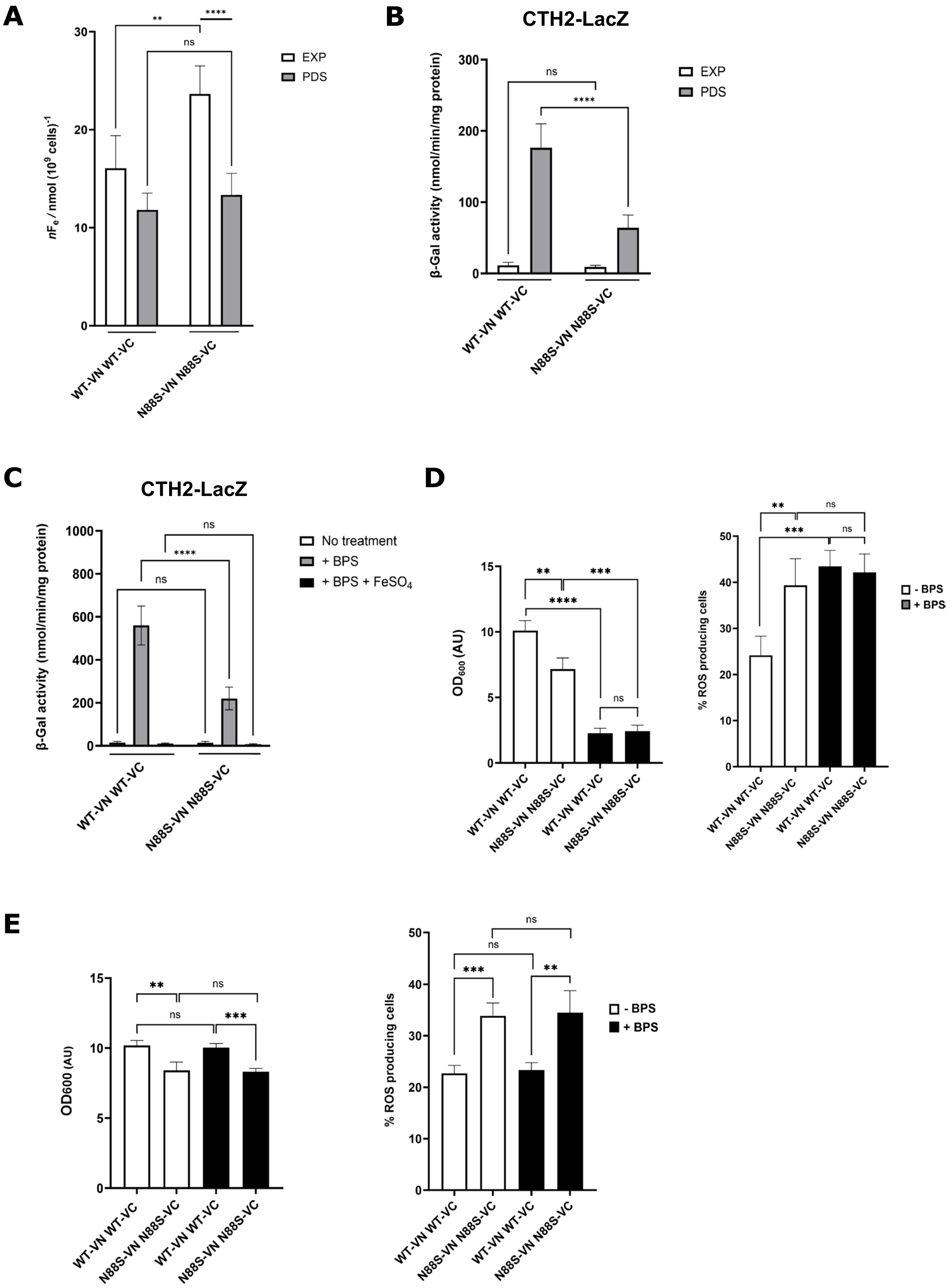

Fig. 5 (See legend on previous page.)

Under iron-rich conditions, around 40% of wild-type cells displayed nuclear Aft1p, whereas only 21% of cells expressing the N88S seipin variant showed nuclear localization of the transcription factor (Fig. 6C). These data suggest increased export of Aft1p to the cytosol, which could explain why full activation of the iron regulon is hampered in the yeast model of N88S seipinopathy.

Hog1p contribution on iron levels and Aft1p transcriptional activity in N88S seipin mutation

We decided to extend our analysis of the contribution of Hog1p to the loss of iron homeostasis imparted by the N88S seipin mutation. Firstly, we measured iron levels during lifespan, and the results revealed that deletion of *HOG1* in WT cells increased iron levels at the exponential phase, consistent with its role as a negative regulator of the iron regulon (Fig. 6D). Importantly, the absence of Hog1p suppressed the iron accumulation phenotype of the mutant, and restored its ability to maintain proper iron levels as observed in WT cells (Fig. 6D). Next, we analyzed the Aft1p transcriptional activity during lifespan and upon BPS treatment in cells expressing p*CTH2*-LacZ. At PDS phase, we observed that deletion of *HOG1* had no significant alterations in the β-galactosidase reporter activity in both WT and N88S seipin-expressing cells (Fig. 6E). This indicates that during lifespan, the activation of the iron regulon by Aft1p/Aft2p is mediated by other signal transduction pathways in addition to Hog1p regulation [34, 35]. However, under iron deprivation, *CTH2*-LacZ expression was induced in WT cells and reached higher levels in the corresponding *hog1*Δ mutant (Fig. 6F). Notably, the transcriptional activity of Aft1p in cells expressing the N88S mutation was restored to WT levels (Fig. 6F) in the absence of the MAPK, supporting the idea that Hog1p controls iron levels and the adaptive response to iron deficiency in the yeast model of N88S seipinopathy.

Hog1p signaling contributes to IB formation in N88S mutant cells

We also decided to investigate whether Hog1p signalling also modulates IB formation in the mutant. For that, we followed intracellular localization of IBs using the Venus signal [43]. We observed a reduction of number of cells displaying IBs upon deletion of either *HOG1* or *SKO1* (Fig. S5A-B), indicating that Hog1p/p38 also promotes IB generation beyond iron imbalance in cells expressing mutant seipin.

Interplay between iron homeostasis and inositol metabolism in N88S seipin-expressing cells

Finally, we decided to investigate if regulation of ER stress response is linked to loss of iron homeostasis observed in the mutant. To test this hypothesis, we analyzed *CTH2*-LacZ reporter activity in cells shifted to SC-glucose medium with or without inositol, supplemented or not with BPS. In WT cells, shifting to inositol-containing medium did not result in measurable changes in the β-galactosidase activity. Notably, *CTH2*-LacZ expression was induced only in the presence of BPS, with no significant changes due to inositol alone in these cells (Fig. S5C). However, in N88S seipin-expressing cells, there was a subtle but consistent increase in Aft1p transcriptional activity when grown in inositol-containing medium supplemented with BPS, compared to cells grown without inositol plus BPS (Fig. S5C). This finding is particularly important as it reveals a previously unexplored functional relationship between inositol and iron metabolism. It indicates that under conditions where PA is consumed and the ER stress response is attenuated in the mutant (Fig. 3E), there is higher activation of the iron regulon by Aft1p/Aft2p in the yeast model of N88S seipinopathy.

(See figure on next page.)

Fig. 6 MAPK Hog1p contributes to iron accumulation and iron dyshomeostasis in cells carrying the N88S seipin mutation under Fe deficiency. **A** Cells with the specified genotypes expressing pMP253 (*CYC1prom-(2xCRE*$_{ENA1}$*)-LacZ*) were grown to reach the exponential phase (EXP) and post-diauxic shift (PDS) phase. Specific β-galactosidase (β-Gal) activities were measured as in Fig. 3A. Two-way ANOVA followed by Šídák's multiple comparison test was used; $n \geq 4$. **B** Western blot showing the phosphorylation and total Aft1p-HA protein levels at the indicated periods of growth. Pgk1p was used as loading control. WT and N88S seipin-expressing cells carrying pRS415-HA-AFT1 were grown in SC-glucose medium during growth and aliquots were collected at different phases as indicated. **C** Cells expressing GFP-AFT1 were grown in SC medium to exponential phase supplemented with 300 μM $FeSO_4$ (II). DAPI was used to stain nuclei. GFP-Aft1p localization and DAPI signal were monitored by fluorescence microscopy (left panel), and quantification of the number of cells with nuclear/cytosolic signal is defined ($n > 100$ cells; right panel). Scale bar, 8 μm. DIC: Differential interference contrast; DAPI- 4′-6-diamidino-2-phenylindole. **D** Total iron levels were measured in the specified cells grown to the specified phases, as described in Fig. 5A. Unpaired *t*-test with Welch´s correction was used; $n \geq 3$. **E**–**F** Cells with the specified genotypes expressing YEplac181-*CTH2*-LacZ were grown as described in Fig. 5B and 5C, respectively. *CTH2*-LacZ associated β-galactosidase (β-Gal) activities were measured as in Fig. 3A. Unpaired *t*-test with Welch´s correction was used; $n \geq 3$. * $p \leq 0.05$; ** $p \leq 0.01$; *** $p \leq 0.001$; **** $p \leq 0.0001$; ns—non-significant

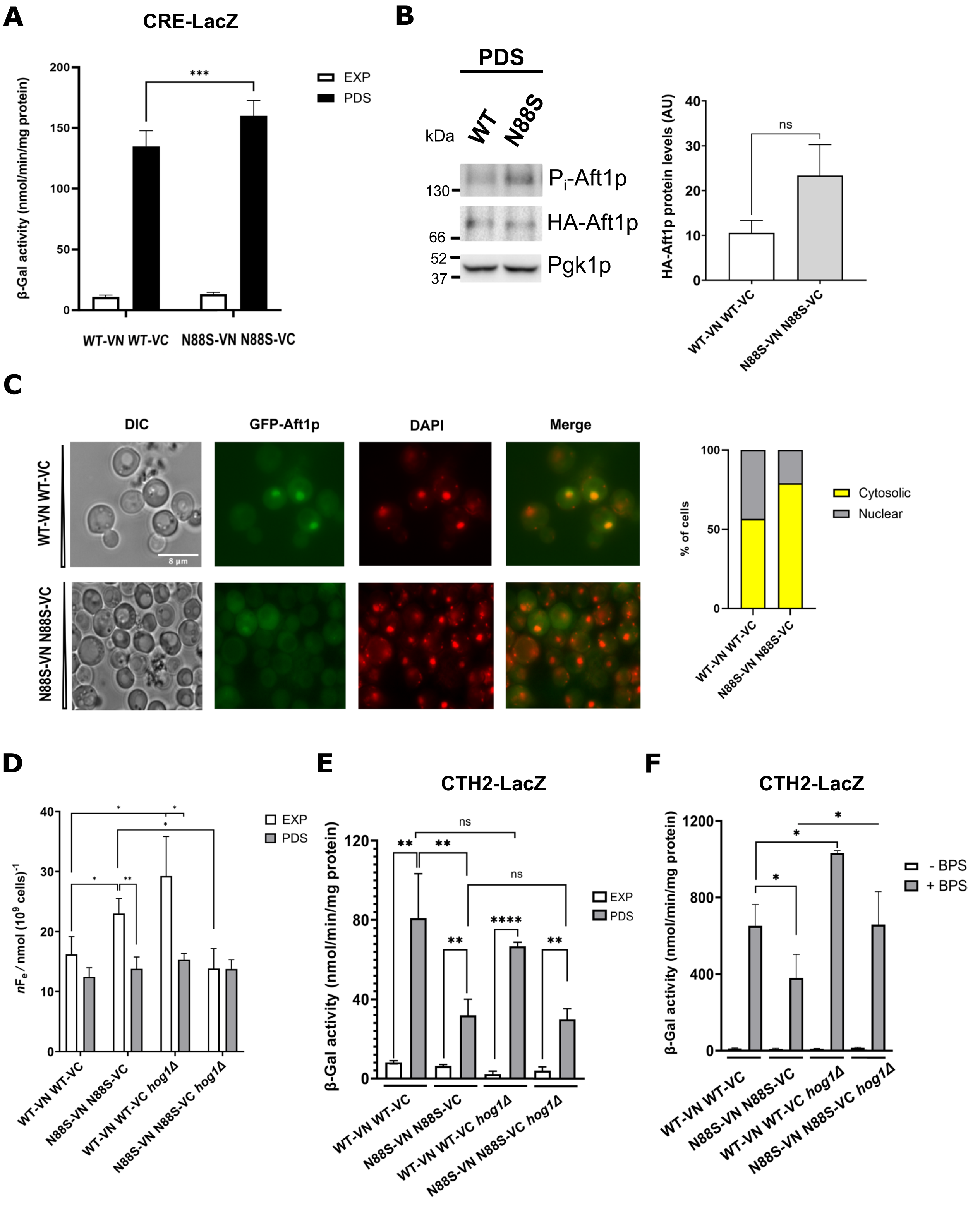

Fig. 6 (See legend on previous page.)

FET3 expression is altered in cells carrying the seipin N88S mutation

The expression of *FET3*, a gene involved in iron uptake, is also regulated by the transcription factor Aft1p [34, 94, 95]. To evaluate if Aft1p inhibition in N88S seipin-expressing cells also affects *FET3* expression, we used a construct containing the *FET3* promoter (-863 bp to + 1) fused to the LacZ reporter gene (YEplac181-*FET3*-LacZ) [49]. In this construct, there is an identified functional Aft1p consensus site [95] located − 254 bp upstream of the ATG translation initiation codon, and a predicted Aft1p-binding site at position − 670 bp (GGCACCC) in the *FET3* promoter [49]. The impact of N88S seipin mutation on *FET3*-LacZ expression was firstly assessed by measuring the β-galactosidase activity of the reporter during lifespan (Fig. 7A). The results showed no differences in the reporter gene expression in WT and N88S seipin-expressing cells at the exponential phase. We observed an increase in *FET3* expression in WT cells at PDS phase, but the induction was higher in the mutant (Fig. 7A), which contrasts with reduced Aft1p-controlled *CTH2* expression observed at the same phase (Fig. 5B). This suggests that in mutant cells, Aft1p regulates *FET3* expression differently compared to other Aft1p-regulated genes.

We also tested if this effect is also observed under BPS-induced iron deficient conditions. As expected, BPS treatment induced *FET3* expression in WT cells, but the reporter fusion activity was even higher in N88S seipin expressing cells (Fig. 7B). Overall, the results indicate that *CTH2* expression was reduced, whereas *FET3* expression is increased at PDS phase and under iron-deficient conditions in cells expressing N88S mutant seipin.

In-silico analysis revealed the presence of a potential Msn2p/Msn4p binding site in the FET3 promoter

Identification of potential Msn2p/Msn4p binding sites in the FET3 promoter

It was previously shown that *FET3* expression is not entirely dependent on Aft1p, and that the transcription factor Ace1p regulates the response to copper overload by limiting the expression of *FET3* [49]. To delineate potential promoter regions responsible for Aft1p-independent activation of *FET3*, we performed an unbiased bioinformatic analysis of the *FET3* promoter (-863 bp to + 1) to search for potential transcription factor binding sites using YEASTRACT + [73]. The results revealed more than 50 transcription factors that could potentially bind to the *FET3* promoter (Table S8). The results identified the putative Aft1p/Aft2p binding sequence (-670 bp), the predicted Ace1p-like binding site (-783 bp) [49], and importantly a Msn2p binding sequence located upstream (-813 bp) on the *FET3* promoter was now uncovered (Fig. 7C).

Msn2/Msn4p regulates FET3 expression in N88S mutant cells

In yeast, the zinc-finger transcription factors Msn2p and Msn4p are key regulators of stress-responsive element (STRE) gene expression [96–101]. Importantly, it was reported that overexpression of the plasma membrane receptor *IZH2* inhibits *FET3* expression via negative regulation of Msn2p/Msn4p transcriptional activation without requiring Aft1p-dependent induction of the iron-responsive element FeRE [102]. Based on this study, we posit that overexpression of *IZH2* should decrease the *FET3*-LacZ reporter gene expression if the latter relies on Msn2p/Msn4p activation. At the exponential phase, no significant differences were observed in all strains tested, but upon transition to PDS phase, we observed higher β-galactosidase activity of the *FET3*-LacZ reporter in cells expressing mutant seipin cells, which was reduced to WT levels upon overexpression of *IZH2* (Fig. 7D). Importantly, we observed a reduction in *FET3* expression in WT cells when *IZH2* was overexpressed (Fig. 7D), which is consistent with a negative regulation of *FET3* expression by Izh2p.

Enhanced Msn2/Msn4p transcriptional activity mirrors higher FET3 expression in N88S mutant cells at PDS phase

In keeping with a role for Msn2p/Msn4p in the regulation of *FET3* expression, we further tested the expression

(See figure on next page.)

Fig. 7 *FET3* expression is more induced at the diauxic shift and under iron deficiency in N88S seipin-expressing cells. **A** Cells with the indicated genotypes expressing YEplac181-*FET3*-LacZ were grown in SC-glucose medium and allowed to grow to reach the exponential phase (EXP) and post-diauxic shift (PDS) phase. Specific β-galactosidase (β-Gal) activities were measured as in Fig. 3A. Unpaired *t*-test with Welch´s correction was used; $n \geq 4$. **B** Overnight precultures of cells with the specified genotypes expressing YEplac181-*FET3*-LacZ were grown in SC-glucose medium to the exponential phase. Cells were incubated with the iron chelator BPS (100 µM) for 4 h to limit iron availability. Specific β-galactosidase (β-Gal) activities were determined as in Fig. 3A. Unpaired *t*-test with Welch´s correction was used; $n = 3$. **C** Schematic representation of the *FET3* promoter. Here, it is displayed the putative Aft1p binding site, the Ace1p-like sequence and the newly identified Msn2p/Msn4p binding sequence. **D** Overnight precultures of cells with the indicated genotypes (cells expressing *IZH2* under the native promoter, or overexpressing *IZH2* under the constitutive GPD promoter) carrying YEplac181-*FET3*-LacZ were grown in SC-glucose medium and allowed to grow to the indicated phases. Specific β-galactosidase (β-Gal) activity was measured as in Fig. 3A. Unpaired *t*-test with Welch´s correction was used; $n \geq 3$. **E** Overnight precultures of cells with the specified genotypes expressing pSTRE-LacZ were grown in SC-glucose medium to reach the EXP, PDS and stationary (STAT) phases. Specific β-galactosidase (β-Gal) activity was measured as in Fig. 3A. Two-way ANOVA followed by Šídák's multiple comparison test was used; $n = 3$. **F** Aconitase activity was measured in PDS-grown cells in SC-glucose medium. Unpaired *t*-test with Welch´s correction was used; $n = 3$. Results are mean ± SD. * $p \leq 0.05$; ** $p \leq 0.01$; *** $p \leq 0.001$; **** $p \leq 0.0001$; ns—non-significant

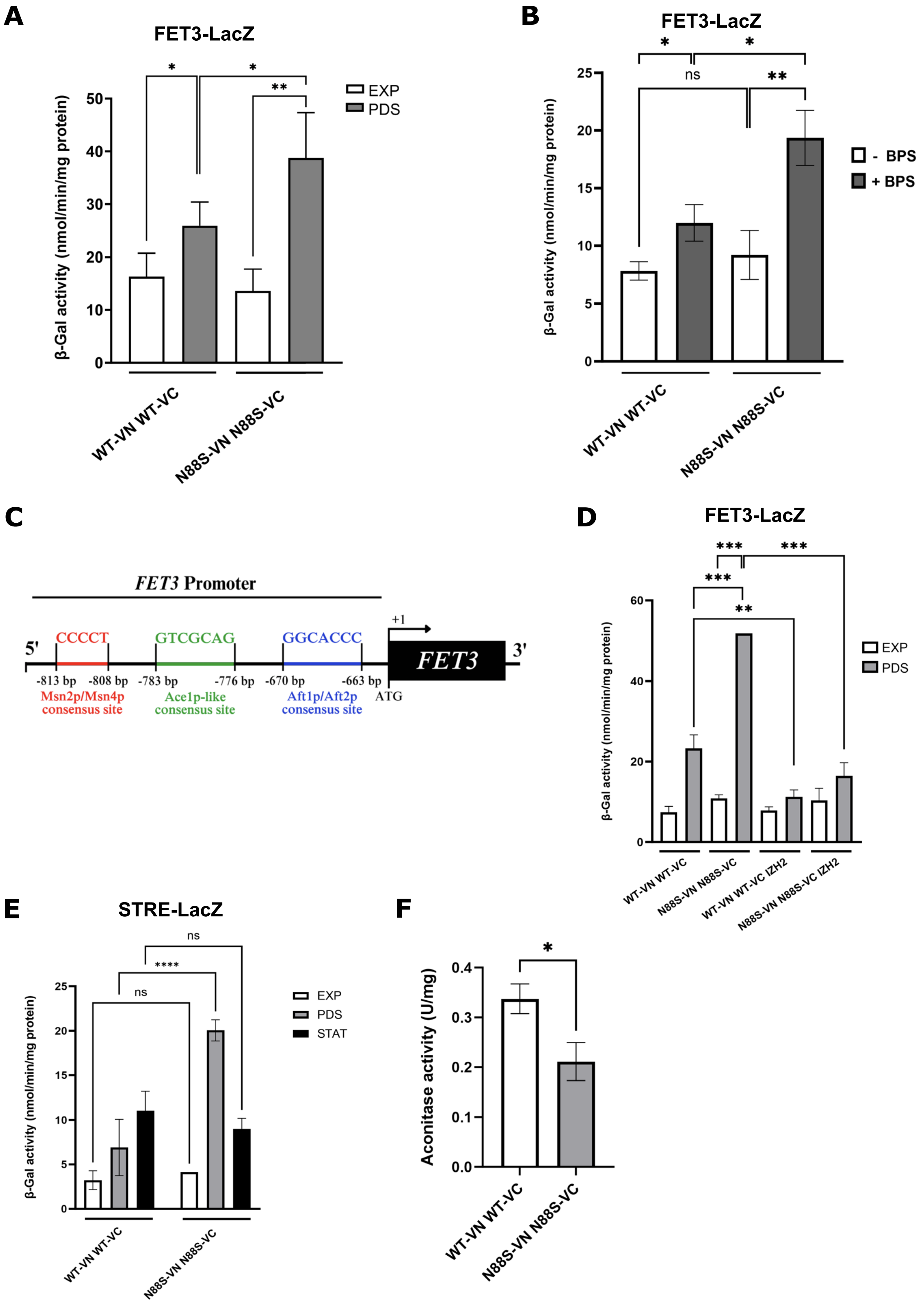

Fig. 7 (See legend on previous page.)

of the pSTRE-LacZ reporter gene, which contains the STRE sequences from the *CTT1* promoter regulated by these transcription factors [103]. Here, we transformed both strains with the reporter, and β-galactosidase activity was measured during lifespan. We found that higher *FET3* expression (Fig. 7A) paralleled the increased activation of Msn2p/Msn4p transcriptional activity at PDS phase in N88S seipin-expressing cells (Fig. 7E).

In addition, a bioinformatic search for target genes with documented regulation by Msn2p/Msn4p identified genes encoding proteins whose levels were found to be higher at PDS phase by proteomic analysis (Table S4), including *GRX2*, *PUT3*, *HXT1*, *HXT7*, *RAS2*, *DIP5*, *ARO10*, *MAL12* and *ARO9* (Table S9). Altogether, the data strongly suggest that stress responsive Msn2p/Msn4p transcription factors are activated and may positively regulate *FET3* expression at PDS phase, thus compensating for the reduced Aft1p transcriptional activity (as observed for *CTH2*-LacZ reporter) in N88S seipin-expressing cells (Fig. 5B). It is possible that *FET3* expression acts as an adaptive response to partially counteract the reduced Aft1p-controlled *CTH2* expression and lower protein levels of Fit1p, Arn1p, Arn2p, and Hmx1p. It is important to note that analysis of the *CTH2* promoter used in the *CTH2*-LacZ reporter fusion [47] did not reveal any binding sites for Msn2p/Msn4p using YEASTRACT + (data not shown).

The induction of *FET3* expression is associated with a reduction in aconitase activity in cells expressing N88S mutant seipin

Cells respond to defective Fe-S cluster synthesis by accumulating iron both within the mitochondria and in the cell. It is known that reducing intracellular iron pool results in decreased activity of the Fe-S cluster enzyme aconitase and subsequently triggers *FET3* expression [104, 105]. Based on this, we measured aconitase activity of WT and N88S seipin-expressing cells grown to PDS phase, when *FET3* expression was increased for the mutant. Aconitase activity was decreased by ~ 40% in the mutant (Fig. 7F), suggesting that mitochondrial Fe-S cluster synthesis/assembly may signal the upregulation of *FET3* expression at PDS phase, while compensating for the reduced activation of the iron regulon by Aft1p, in an attempt to reestablish homeostatic intracellular iron levels. In agreement with this hypothesis, we observed that many genes involved in Fe-S cluster assembly were among the most affected DEGs in cells expressing the N88S seipin mutation under conditions of Fe deprivation (Fig. S4D).

Discussion

Altered phospholipid metabolism and PA accumulation in N88S seipin-expressing cells

In this project, we provide evidence that inositol and neutral lipid metabolism and cellular iron homeostasis are compromised in the yeast model of N88S seipinopathy (Fig. 8). Importantly, our results are consistent with a reduced rate of phospholipid biosynthesis coupled with PA accumulation. As a result, the activity of the Opi1p transcriptional repressor is impaired, leading to derepression of *INO1* expression and increased levels of Ino1p. Nevertheless, we did not observe altered levels of major phospholipids, including PC, PG, PE, PS or PI. It has been previously reported that about 10% of the WT level of activity of the phospholipid biosynthetic enzymes is sufficient to maintain normal growth and almost normal lipid composition [28, 84, 106]. However, a decrease in the protein levels of these enzymes is expected to significantly influence the flux of lipid precursor at the PA metabolic branch point, where PA can also be channeled towards TG synthesis at the expense of a reduced rate of de novo synthesis of phospholipids (Fig. 8). Finally, it is interesting to observe that the deletion of *SEI1* or *LDB16* also leads to a PA buildup at the nuclear ER, and that aberrant supersized LD is also a result of altered phospholipid metabolism [107, 108]. Notably, heterologous expression of the human N88S seipin mutation in a seipin-null strain also leads to changes in LD size and number when compared to its human WT counterpart [6, 109], which may similarly stem from disruptions in PA and phospholipid metabolism, as discussed in this study. Notably, similar misregulation of Opi1p-mediated transcriptional activity observed in the N88S mutant was previously reported for the *ldb16* mutant. [110]. Overall, these results indicate that the N88S mutation closely mimics several abnormalities in phospholipid and inositol metabolism observed in seipin mutants, further emphasizing seipin's essential role in PA remodeling and its downstream effects on lipid metabolism. PA increases membrane order in the ER, and its accumulation has been associated with the induction of the ER stress response and apoptosis under various conditions [111, 112]. It would then be interesting to further explore whether changes in ER ultrastructure could also contribute to ER stress beyond IB formation associated with seipin misfolding.

Lysophospholipids as potential biomarkers and therapeutic targets for N88S seipinopathy

Remarkably, we observed increased levels of lysophospholipids, indicating that lysophospholipid:acyl-CoA acyltransferases (LPLATs) Slc1p and Ale1p activities are likely impaired. Of particular interest, dysfunction in LPA signaling has been associated with several neurological conditions, including Alzheimer's disease and Parkinson's disease, and other disorders [113–115]. Moreover, LPC has been shown to contribute to pericyte loss, disruption of the vascular barrier, demyelination,

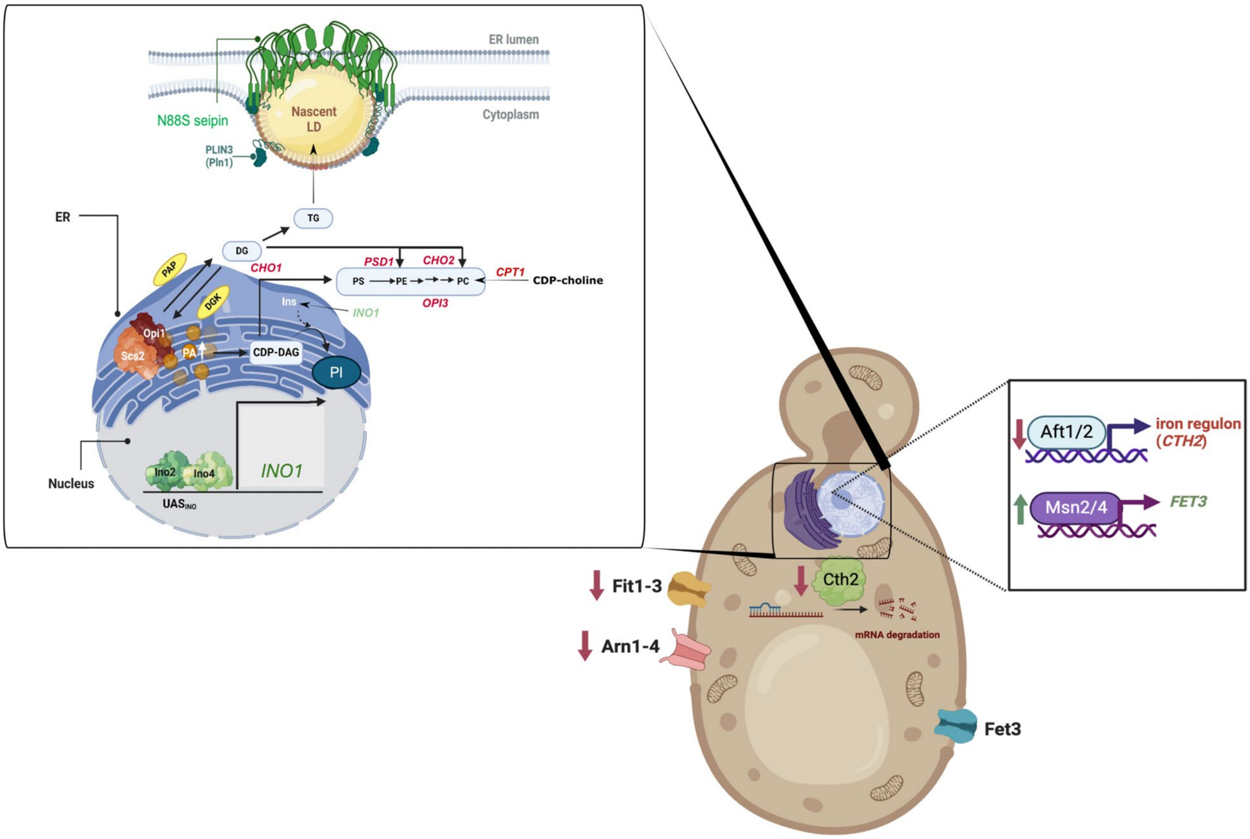

Fig. 8 Uncovering iron imbalance and inositol metabolism disruption: insights from the yeast model of N88S seipinopathy. In this model system, there is an accumulation of PA associated with derepressed *INO1* expression, along with reduced protein levels of key enzymes in the phospholipid biosynthetic pathway. This dysregulation is accompanied by an increase in triglyceride (TG) levels in cells expressing the N88S mutation. Whereas WT cells normally upregulate *CTH2* and *FET3* expression during the diauxic shift, responding to increased iron demand, cells expressing N88S seipin exhibit impaired Aft1p/Aft2p transcriptional activity, leading to reduced levels of iron transport and storage proteins such as Fit1p, Arn1p, Arn2p, and Hmx1p. This results in iron dyshomeostasis, particularly under iron-deficient conditions. The activation of the stress response via transcription factors Msn2p/Msn4p may provide an adaptive mechanism to better manage iron deficiency during the transition to the post-diauxic shift. This adaptation potentially allows cells to bypass the reduced function of Aft1p/Aft2p on the iron regulon, thereby enhancing iron assimilation through the reductive pathway. This pathway involves the reduction of ferric to ferrous ions and the protein complex formed by the Ftr1p transporter and the Fet3p ferroxidase. Moreover, we propose that *FET3* expression is linked to potential disruptions in Fe-S cluster activity and/or assembly in cells carrying the N88S seipin mutation. This is supported by the observed reduction in aconitase activity, which relies on an intact [4Fe-4S] cluster for full functionality. Our findings indicate that human N88S seipinopathy might be both a proteinopathy and a lipidopathy, with disruption in inositol and lipid metabolism playing a significant role in triggering the ER stress response. Furthermore, the resulting iron imbalance may impair various cellular functions, including antioxidant mechanisms like catalase, and could contribute to the progression of neurodegenerative traits observed in human disease. Images were generated using bioRender. Green and red indicates upregulated and downregulated, respectively

and motor function impairments [116–118]. Additionally, LPC exacerbates the neurotoxicity of amyloid β1-42 peptide oligomer formation and promotes neurotoxic protein aggregation, highlighting its potential as a therapeutic target for neurodegenerative diseases [119, 120]. Notably, one study found that patients with repetitive mild traumatic brain injury exhibited significantly elevated LPC levels [121]. Unfortunately, search for diagnostic and prognostic biomarkers in seipinopathy and related MNDs is scarce, and there are currently no definitive molecular biomarkers associated with such disorders. Here, we propose that PA and lysophospholipids could serve as potential candidates for biomarkers of this cohort of diseases.

N88S seipinopathy as a proteinopathy and lipidopathy

Overall, we provide strong evidence that N88S seipinopathy is also a lipidopathy. In fact, deletion of *INO1* increased basal levels of the ER stress response, however this was associated with reduced IB formation in N88S seipin-expressing cells. It should be noted that *INO1* deletion did not affect ROS levels in mutant cells, suggesting that oxidative stress is not directly linked to lipid metabolism defects. In line with abnormal lipid profile observed in cells expressing N88S seipin, which influences the activation of the ER stress response, we posit that an imbalance in cellular lipid homeostasis is a potential major driver of the neurotoxic process in human seipinopathy, with N88S seipin misfolding acting as the initiating trigger. This aligns with seipin´s crucial role in phospholipid and neutral lipid metabolism. However, we cannot exclude the possibility that seipinopathy and related human MNDs may be defined as both proteinopathies and lipidopathies. A vicious cycle of dysregulation in protein folding and lipid metabolism might be initiated by early and subtle changes in either lipid or protein handling as previously proposed [43].

Disruption of iron homeostasis is a hallmark the yeast model of N88S seipinopathy

Another interesting finding of this work was the loss of iron homeostasis in the yeast model of N88S seipinopathy (Fig. 8). Our proteomic analysis revealed that levels of iron homeostasis-associated proteins, including Fit1p, Arn1p, Arn2p, and Hmx1p, were reduced in cells expressing the N88S seipin mutation. The expression of these proteins is regulated by the major iron-sensing transcription factor Aft1p, a key transcription factor that manages the cellular response to iron deficiency. In this study, it was shown that Aft1p transcriptional activity is deregulated during lifespan and upon iron depletion, which likely contributes to a defective adaptive response, particularly under conditions of iron deficiency. We provide strong evidence that Aft1p localization was impaired under excess iron conditions, and importantly MAPK Hog1p/p38 was involved in the regulation of *CTH2* expression in response to iron starvation, but not throughout lifespan. This indicates that other major signaling effectors (e.g., Snf1p/AMPK or PKA) might control the transcription of genes belonging to the iron regulon via regulation of Aft1p activation and its transcriptional activity [34, 35]. Yet, we found that the expression of the ferroxidase Fet3p, which is required for high affinity iron transport and also regulated by Aft1p, was increased. While both Cth1p and Cth2p are transcriptionally induced by Aft1p/Aft2p, *FET3* expression appears to be adaptively regulated by multiple transcription factors in response to changes in iron and other ion levels, including Ace1p, Aft1p and Msn2p. Importantly, Cth1/2p functions post-transcriptionally by targeting and degrading RNA transcripts of nonessential proteins that require large amounts of iron [47]. In contrast, Fet3p operates upstream by capturing iron to fulfil cellular iron needs, with its expression being more closely associated with the iron-sulfur (Fe-S) biogenesis machinery [104, 105]. Notably, defects in the assembly of cytosolic Fe-S cluster-containing proteins do not trigger activation of the iron regulon. Instead, alterations in mitochondrial iron-sulfur cluster assembly are important for signaling iron bioavailability to Aft1p or Aft2p [122, 123]. The activity of the mitochondrial Fe-S enzyme aconitase was inversely correlated with the expression of *FET3* in the mutant, in agreement with previous findings [105]. We currently envision a model where coupling transcription of the high affinity iron transport system Ftr1p/Fet3p to the Fe-S cluster activity may provide a potential link that might explain why *FET3* expression increased via activation of stress responsive transcription factors Msn2p/Msn4p (Fig. 8), despite reduced Aft1p transcriptional activity and iron imbalance. Moreover, it is known that Fe-S clusters are primary targets of ROS, so impaired Fe-S metabolism, as suggested by partial loss of aconitase activity, could potentially contribute to ROS buildup and oxidative damage exhibited by the N88S mutant strain [43]. Loss of aconitase activity may therefore reflect increased levels of cellular dysfunction due to oxidative damage or possibly changes in other cellular processes, as recently proposed for Parkinson´s disease [124]. This could be relevant to human N88S seipinopathy pathogenesis as a biomarker candidate to improve diagnostics/disease progression. Whether mitochondrial mobilization of iron coupled with the synthesis of Fe-S clusters is altered in N88S seipin-expressing cells is currently undefined, and should be explored in future studies.

Limitations of the yeast model for motor neuropathy studies

Yeast and human cells exhibit fundamental differences in lipid metabolism and iron homeostasis, reflecting their distinct biological contexts. While yeast relies heavily on de novo phospholipid synthesis and lacks certain mammalian phospholipid remodeling pathways, human cells also exhibit tissue-specific lipid profiles and systemic regulatory mechanisms involving apoliproteins. Similarly, yeast utilizes a robust iron regulon primarily governed by Aft1p/Aft2p for iron acquisition and intracellular distribution, whereas human iron homeostasis involves intricate systemic coordination, through proteins like transferrin and ferritin, and via hepcidin, tailored to meet multicellular demands. Yeast's unicellular nature limits its ability to capture and model complex intercellular interactions and tissue-specific features critical for understanding motor neuropathies, such as neuron-glia lipid and metabolic coupling, brain iron and redox balance, and neurodegeneration. Despite these limitations, humanized yeast models have proven valuable for identifying therapeutic targets, biomarkers, drug discovery and disease functional networks, establishing their utility in studying human disorders as in this work. However, validation in mammalian models is essential to confirm biological relevance to motor neuropathy.

Conclusions

This study presents compelling evidence that human N88S seipinopathy may also be a lipidopathy linked to the disruption of iron homeostasis. The accumulation of PA, combined with a decreased rate of phospholipid synthesis, plays a crucial role in inducing ER stress. Restoring inositol metabolism or modulating PA synthesis has the potential to alleviate ER stress, regulate IB formation, and improve phospholipid biosynthesis defects. Notably, studies have demonstrated the beneficial effects of *myo*-inositol dietary supplementation in various disorders linked to inositol imbalance [125]. Additionally, the impaired ability of N88S mutant cells to cope with iron deficiency likely disrupts the Krebs cycle, weakens antioxidant defenses, and affects Fe-S cluster enzyme activity, as evidenced by reduced catalase and aconitase activity in this yeast model of the disease [43]. Therapeutic strategies ranging from direct antioxidant supplementation to gene therapy aimed at enhancing endogenous catalase activity could prove promising for seipinopathies and related MNDs [126]. Similar to yeast, mammalian systems respond to iron deficiency through post-transcriptional and metabolic reprogramming, facilitated by the IRP-IRE signaling pathway, which maintains iron homeostasis [127]. Given its therapeutic relevance in neurodegenerative diseases [127], we propose that modulation of this pathway and/or controlled iron supplementation, via dietary or pharmacological approaches, may represent viable strategies for addressing seipinopathies therapeutically. To the best of our knowledge, this study represents the first detailed description of protein and lipid alterations in N88S seipinopathy using systems biology.

Abbreviations

ACAT	Acyl-coenzyme A: cholesterol acyltransferase
AGPAT	Acylglycerolphosphate Acyltransferase
BiFC	Biomolecular Fluorescence Complementation
BPS	Bathophenanthrolinesulfonate
BSCL2	Berardinelli-Seip congenital lipodystrophy type 2
CDP-DAG	Cytidine Diphosphate-Diacylglycerol
CYC1t	CYC1 terminator
DEG	Differentially Expressed Genes
DEP	Differentially Expressed Protein
DG	Diacylglycerol
DGAT	Acyl-CoA Diacylglycerol Acyltransferase
DNA	Deoxyribonucleic Acid
ER	Endoplasmic Reticulum
ERAD	ER-Associated Degradation
EXP	Exponential Phase
Fe-S	Iron-Sulfur
FIT	Fat storage-inducing transmembrane
GO	Gene Ontology
GPAT	Glycerol-3 Phosphate Acyltransferase
GPDpr	GPD promoter
IB	Inclusion body
IREB2	Iron Responsive Element Binding Protein 2
LA	Lithium Acetate
LD	Lipid Droplet
LPA	Lysophosphatidic Acid
LPC	Lysophosphatidylcholine
LPLAT	Lysophospholipid:acyl-CoA acyltransferases
MAPK	Mitogen-Activated Protein Kinase
MNDs	Motor Neuron Diseases
MS	Mass Spectrometry
ONPG	O-nitrophenylgalactopyranosyde
PA	Phosphatidic Acid
PC	Phosphatidylcholine
PE	Phosphatidylethanolamine
PG	Phosphatidylglycerol
PI	Phosphatidylinositol
PS	Phosphatidylserine
PDS	Post-diauxic shift
PEG	Polyethylene glycol
ROS	Reactive Oxygen Species
SC	Synthetic Complete
SE	Sterol Esters
STRE	Stress Response Element
TFs	Transcription Factors
TG	Triacylglycerol
UPR	Unfolded Protein Response
VC	Venus C-terminal fragment
VN	Venus N-terminal fragment
WT	Wild-type
YNB	Yeast Nitrogen Base
YPD	Yeast Peptone Dextrose

Supplementary Information

The online version contains supplementary material available at https://doi.org/10.1186/s12964-024-02007-9.

Supplementary Material 1: Figure S1. (A) Cluster analysis of protein abundance profiles of WT and N88S seipin-expressing cells (for the 3 independent experiments for each strain) grown to post-diauxic shift (PDS) phase in SC-glucose medium. Blue indicates downregulation, red indicates upregulation and white indicates no detectable change. (B) Statistics of significantly enriched KEGG pathways of differentially expressed proteins (DEPs). (C) Detailed pathway enrichment analysis of DEPs based on KEGG database.

Supplementary Material 2: Figure S2. (A) Cluster analysis of lipid abundance profiles in WT and N88S seipin-expressing cells (for the 3 independent experiments for each strain). Purple indicates downregulation, red indicates upregulation and white indicates no detectable change. (B) Bubble diagram of differential lipids in N88S seipin-expressing cells. The abscissa is the fold change after log*2* conversion, and the ordinate is the lipid subclass. (C-F) Levels of fatty acids, ceramide, PA (34:1) and phosphatidylinositol phosphates (PIPs), respectively, in WT and mutant cells. Results are mean±SD (n=3). All fatty acids (excluding the 38:2) and ceramide levels were not statistically different in N88S vs WT cells. * $p \leq 0.05$; ** $p \leq 0.01$ (unpaired *t*-test with Welch´s correction).

Supplementary Material 3: Figure S3. (A) Cells with the indicated genotypes were grown in SC-glucose medium until stationary phase, and ROS levels were assessed in cells labeled with dihydroethidium (DHE) via flow cytometry using the FL3 channel. Results are mean±SD. * $p \leq 0.05$; **** $p \leq 0.0001$; ns - non-significant (unpaired *t*-test with Welch´s correction was used; $n \geq 3$).

Supplementary Material 4: Figure S4. (A) The KEGG enriched pathways and GO terms of differentially expressed genes (DEGs) in bathophenanthrolinedisulfonate/BPS-treated cells carrying the N88S seipin mutation compared to BPS-treated WT cells, as described in Material and Methods (2.5). (B-D) GO enrichment bubble chart for biological process (B), cellular component (C) and molecular function (D). The X-axis represents the enrichment ratio, and the Y-axis represents the GO Term. The size of the bubble represents the number of differential genes annotated to a certain GO Term. The color represents the significance value of enrichment (Q-value), where red indicates smaller significance values. (E) Venn diagram charts of DEGs. The upper graph corresponds to the number of overlapping genes (10) whose expression was found to be upregulated by iron depletion (28, blue) as in (1), but represents downregulated DEGs in N88S seipin-expressing cells (197, orange). The lower graph depicts the number of overlapping genes (13) whose expression was found to be downregulated by iron depletion (34, blue) as in (1), but corresponds to upregulated DEGs in N88S seipin-expressing cells (250, orange). The coverage is approximately 36-38%. (1) Puig S, Askeland E, Thiele DJ. Coordinated remodeling of cellular metabolism during iron deficiency through targeted mRNA degradation. Cell. 2005;120(1):99-110.

Supplementary Material 5: Figure S5. (A-B) Formation of IBs was monitored by fluorescence microscopy using the YFP/Venus channel (left panel) in cells grown to the exponential phase in SC-glucose medium. Quantification is defined as percentage of cells displaying IB foci (n>100 cells, right panel). Data were combined from 2 independent experiments. DIC: Differential interference contrast. Bar scale, 8 µm. (C) Cells with the specified genotypes expressing YEplac181-*CTH2*-LacZ were grown in SC-glucose medium lacking inositol to the exponential phase. Cells were then shifted to fresh SC-glucose medium with or without inositol (1 mM), supplemented or not with BPS (100 µM), as indicated, and incubated for an additional 2 h. Protein extracts were prepared, and specific β-galactosidase (β-Gal) activities, with *o*-nitrophenyl-β-D-galactopyranoside (ONPG) as a substrate, were determined by measuring the amount of o-nitrophenol released by the galactosidase-catalyzed hydrolysis process. Two-way ANOVA followed by Šídák's multiple comparison test was used; n=3. *** $p \leq 0.001$; ns - non-significant.

Supplementary Material 6.

Acknowledgements
We would like to thank the YSN Group for productive discussions and the i3S Scientific Platforms and BGI commercial services for their technical assistance with bioinformatic analysis, flow cytometry, fluorescence microscopy, and omics approaches used in this study.

Authors' contributions
V. T. and V. C. conceived and supervised the project. V. T. and V. C. designed the experiments and analyzed most of the data. M. R., M. O. and V. N. performed most of the experiments. V. T. wrote the manuscript with input from all authors.

Funding
This work was funded by national funds through Foundation for Science and Technology (FCT), under the project UIDB/04293/2020, under the project 2022.02305.PTDC, CEECIND/00724/2017 and CEECIND/00724/2017/CP1386/CT0006, and EMBO Scientific Exchange Grant 9890.

Data Availability
No datasets were generated or analysed during the current study.

Declarations

Competing interests
The authors declare no competing interests.

Author details
[1]IBMC - Instituto de Biologia Molecular E Celular, University of Porto, Porto, Portugal. [2]Yeast Signalling Networks (YSN), i3S - Instituto de Investigação E Inovação Em Saúde, University of Porto, Porto, Portugal. [3]Department of Molecular Biology, ICBAS - Instituto de Ciências Biomédicas Abel Salazar, School of Medicine and Biomedical Sciences, Universidade Do Porto, Porto, Portugal.

Received: 8 October 2024 Accepted: 21 December 2024

References

1. Zadoorian A, Du X, Yang H. Lipid droplet biogenesis and functions in health and disease. Nat Rev Endocrinol. 2023;19(8):443–59.
2. Rakotonirina-Ricquebourg R, Costa V, Teixeira V. Hello from the other side: Membrane contact of lipid droplets with other organelles and subsequent functional implications. Prog Lipid Res. 2022;85:101141.
3. Henne W. The Molecular Era of Lipid Droplets. Contact. 2020;3:1–9.
4. Yan R, Qian H, Lukmantara I, Gao M, Du X, Yan N, Yang H. Human SEIPIN Binds Anionic Phospholipids. Dev Cell. 2018;47(2):248-56 e4.
5. Combot Y, Salo VT, Chadeuf G, Holtta M, Ven K, Pulli I, et al. Seipin localizes at endoplasmic-reticulum-mitochondria contact sites to control mitochondrial calcium import and metabolism in adipocytes. Cell Rep. 2022;38(2):110213.
6. Fei W, Shui G, Gaeta B, Du X, Kuerschner L, Li P, et al. Fld1p, a functional homologue of human seipin, regulates the size of lipid droplets in yeast. J Cell Biol. 2008;180(3):473–82.
7. Klug YA, Deme JC, Corey RA, Renne MF, Stansfeld PJ, Lea SM, Carvalho P. Mechanism of lipid droplet formation by the yeast Sei1/Ldb16 Seipin complex. Nat Commun. 2021;12(1):5892.
8. Arlt H, Sui X, Folger B, Adams C, Chen X, Remme R, et al. Seipin forms a flexible cage at lipid droplet formation sites. Nat Struct Mol Biol. 2022;29(3):194–202.
9. Binns D, Lee S, Hilton CL, Jiang QX, Goodman JM. Seipin is a discrete homooligomer. Biochemistry. 2010;49(50):10747–55.
10. Grippa A, Buxo L, Mora G, Funaya C, Idrissi FZ, Mancuso F, et al. The seipin complex Fld1/Ldb16 stabilizes ER-lipid droplet contact sites. J Cell Biol. 2015;211(4):829–44.
11. Fei W, Shui G, Zhang Y, Krahmer N, Ferguson C, Kapterian TS, et al. A role for phosphatidic acid in the formation of "supersized" lipid droplets. PLoS Genet. 2011;7(7):e1002201.
12. Salo VT, Belevich I, Li S, Karhinen L, Vihinen H, Vigouroux C, et al. Seipin regulates ER-lipid droplet contacts and cargo delivery. EMBO J. 2016;35(24):2699–716.
13. Szymanski KM, Binns D, Bartz R, Grishin NV, Li WP, Agarwal AK, et al. The lipodystrophy protein seipin is found at endoplasmic reticulum lipid droplet junctions and is important for droplet morphology. Proc Natl Acad Sci U S A. 2007;104(52):20890–5.
14. Ito D, Fujisawa T, Iida H, Suzuki N. Characterization of seipin/BSCL2, a protein associated with spastic paraplegia 17. Neurobiol Dis. 2008;31(2):266–77.
15. Windpassinger C, Auer-Grumbach M, Irobi J, Patel H, Petek E, Horl G, et al. Heterozygous missense mutations in BSCL2 are associated with distal hereditary motor neuropathy and Silver syndrome. Nat Genet. 2004;36(3):271–6.
16. Auer-Grumbach M, Schlotter-Weigel B, Lochmuller H, Strobl-Wildemann G, Auer-Grumbach P, Fischer R, et al. Phenotypes of the N88S Berardinelli-Seip congenital lipodystrophy 2 mutation. Ann Neurol. 2005;57(3):415–24.
17. Teixeira V, Maciel P, Costa V. Leading the way in the nervous system: Lipid Droplets as new players in health and disease. Biochim Biophys Acta Mol Cell Biol Lipids. 2021;1866(1):158820.
18. van de Warrenburg BP, Scheffer H, van Eijk JJ, Versteeg MH, Kremer H, Zwarts MJ, et al. BSCL2 mutations in two Dutch families with overlapping Silver syndrome-distal hereditary motor neuropathy. Neuromuscul Disord. 2006;16(2):122–5.
19. Ito D, Yagi T, Suzuki N. BSCL2-related neurologic disorders/seipinopathy: endoplasmic reticulum stress in neurodegeneration. Rinsho Shinkeigaku. 2011;51(11):1186–8.
20. Ito D, Yagi T, Ikawa M, Suzuki N. Characterization of inclusion bodies with cytoprotective properties formed by seipinopathy-linked mutant seipin. Hum Mol Genet. 2012;21(3):635–46.
21. Yagi T, Ito D, Nihei Y, Ishihara T, Suzuki N. N88S seipin mutant transgenic mice develop features of seipinopathy/BSCL2-related motor neuron disease via endoplasmic reticulum stress. Hum Mol Genet. 2011;20(19):3831–40.
22. Ito D, Suzuki N. Molecular pathogenesis of seipin/BSCL2-related motor neuron diseases. Ann Neurol. 2007;61(3):237–50.
23. Carman GM, Han GS. Regulation of phospholipid synthesis in the yeast Saccharomyces cerevisiae. Annu Rev Biochem. 2011;80:859–83.
24. Santiago TC, Mamoun CB. Genome expression analysis in yeast reveals novel transcriptional regulation by inositol and choline and

new regulatory functions for Opi1p, Ino2p, and Ino4p. J Biol Chem. 2003;278(40):38723–30.
25. Lopes JM, Henry SA. Interaction of trans and cis regulatory elements in the INO1 promoter of Saccharomyces cerevisiae. Nucleic Acids Res. 1991;19(14):3987–94.
26. Loewen CJ, Gaspar ML, Jesch SA, Delon C, Ktistakis NT, Henry SA, Levine TP. Phospholipid metabolism regulated by a transcription factor sensing phosphatidic acid. Science. 2004;304(5677):1644–7.
27. Jesch SA, Zhao X, Wells MT, Henry SA. Genome-wide analysis reveals inositol, not choline, as the major effector of Ino2p-Ino4p and unfolded protein response target gene expression in yeast. J Biol Chem. 2005;280(10):9106–18.
28. Henry SA, Gaspar ML, Jesch SA. The response to inositol: regulation of glycerolipid metabolism and stress response signaling in yeast. Chem Phys Lipids. 2014;180:23–43.
29. Loewen CJ, Levine TP. A highly conserved binding site in vesicle-associated membrane protein-associated protein (VAP) for the FFAT motif of lipid-binding proteins. J Biol Chem. 2005;280(14):14097–104.
30. Hofbauer HF, Gecht M, Fischer SC, Seybert A, Frangakis AS, Stelzer EHK, et al. The molecular recognition of phosphatidic acid by an amphipathic helix in Opi1. J Cell Biol. 2018;217(9):3109–26.
31. Belaidi AA, Bush AI. Iron neurochemistry in Alzheimer's disease and Parkinson's disease: targets for therapeutics. J Neurochem. 2016;139(Suppl 1):179–97.
32. Li L, Ward DM. Iron toxicity in yeast: transcriptional regulation of the vacuolar iron importer Ccc1. Curr Genet. 2018;64(2):413–6.
33. Ramos-Alonso L, Romero AM, Martinez-Pastor MT, Puig S. Iron Regulatory Mechanisms in Saccharomyces cerevisiae. Front Microbiol. 2020;11:582830.
34. Martinez-Pastor MT, Perea-Garcia A, Puig S. Mechanisms of iron sensing and regulation in the yeast Saccharomyces cerevisiae. World J Microbiol Biotechnol. 2017;33(4):75.
35. Martins TS, Costa V, Pereira C. Signaling pathways governing iron homeostasis in budding yeast. Mol Microbiol. 2018;109(4):422–32.
36. Philpott CC, Protchenko O. Response to iron deprivation in Saccharomyces cerevisiae. Eukaryot Cell. 2008;7(1):20–7.
37. Protchenko O, Philpott CC. Regulation of intracellular heme levels by HMX1, a homologue of heme oxygenase. Saccharomyces cerevisiae J Biol Chem. 2003;278(38):36582–7.
38. Ojeda L, Keller G, Muhlenhoff U, Rutherford JC, Lill R, Winge DR. Role of glutaredoxin-3 and glutaredoxin-4 in the iron regulation of the Aft1 transcriptional activator in Saccharomyces cerevisiae. J Biol Chem. 2006;281(26):17661–9.
39. Pujol-Carrion N, Belli G, Herrero E, Nogues A, de la Torre-Ruiz MA. Glutaredoxins Grx3 and Grx4 regulate nuclear localisation of Aft1 and the oxidative stress response in Saccharomyces cerevisiae. J Cell Sci. 2006;119(Pt 21):4554–64.
40. Martins TS, Pereira C, Canadell D, Vilaca R, Teixeira V, Moradas-Ferreira P, et al. The Hog1p kinase regulates Aft1p transcription factor to control iron accumulation. Biochim Biophys Acta Mol Cell Biol Lipids. 2018;1863(1):61–70.
41. Pujol-Carrion N, Pavon-Verges M, Arroyo J, de la Torre-Ruiz MA. The MAPK Slt2/Mpk1 plays a role in iron homeostasis through direct regulation of the transcription factor Aft1. Biochim Biophys Acta Mol Cell Res. 2021;1868(5):118974.
42. Guo J, Qiu W, Soh SL, Wei S, Radda GK, Ong WY, et al. Motor neuron degeneration in a mouse model of seipinopathy. Cell Death Dis. 2013;4:e535.
43. Nogueira V, Chang CK, Lan CY, Pereira C, Costa V, Teixeira V. Causative links between ER stress and oxidative damage in a yeast model of human N88S seipinopathy. Free Radic Biol Med. 2022;192:165–81.
44. Janke C, Magiera MM, Rathfelder N, Taxis C, Reber S, Maekawa H, et al. A versatile toolbox for PCR-based tagging of yeast genes: new fluorescent proteins, more markers and promoter substitution cassettes. Yeast. 2004;21(11):947–62.
45. Longtine MS, McKenzie A 3rd, Demarini DJ, Shah NG, Wach A, Brachat A, et al. Additional modules for versatile and economical PCR-based gene deletion and modification in Saccharomyces cerevisiae. Yeast. 1998;14(10):953–61.
46. Yofe I, Schuldiner M. Primers-4-Yeast: a comprehensive web tool for planning primers for Saccharomyces cerevisiae. Yeast. 2014;31(2):77–80.
47. Puig S, Askeland E, Thiele DJ. Coordinated remodeling of cellular metabolism during iron deficiency through targeted mRNA degradation. Cell. 2005;120(1):99–110.
48. Li D, Yang SG, He CW, Zhang ZT, Liang Y, Li H, et al. Excess diacylglycerol at the endoplasmic reticulum disrupts endomembrane homeostasis and autophagy. BMC Biol. 2020;18(1):107.
49. Gaspar-Cordeiro A, Marques Caetano S, Amaral C, Rodrigues-Pousada C, Pimentel C. Ace1 prevents intracellular copper accumulation by regulating Fet3 expression and thereby restricting Aft1 activity. FEBS J. 2018;285(10):1861–72.
50. Crisp RJ, Pollington A, Galea C, Jaron S, Yamaguchi-Iwai Y, Kaplan J. Inhibition of heme biosynthesis prevents transcription of iron uptake genes in yeast. J Biol Chem. 2003;278(46):45499–506.
51. Gietz RD, Schiestl RH. Large-scale high-efficiency yeast transformation using the LiAc/SS carrier DNA/PEG method. Nat Protoc. 2007;2(1):38–41.
52. Hong H, Shen R, Zhang F, Wen Z, Chang S, Lin W, et al. The complex effects of ocean acidification on the prominent N(2)-fixing cyanobacterium Trichodesmium. Science. 2017;356(6337):527–31.
53. Perez-Riverol Y, Bai J, Bandla C, Garcia-Seisdedos D, Hewapathirana S, Kamatchinathan S, et al. The PRIDE database resources in 2022: a hub for mass spectrometry-based proteomics evidences. Nucleic Acids Res. 2022;50(D1):D543–52.
54. Wen B, Zhou R, Feng Q, Wang Q, Wang J, Liu S. IQuant: an automated pipeline for quantitative proteomics based upon isobaric tags. Proteomics. 2014;14(20):2280–5.
55. Savitski MM, Wilhelm M, Hahne H, Kuster B, Bantscheff M. A Scalable Approach for Protein False Discovery Rate Estimation in Large Proteomic Data Sets. Mol Cell Proteomics. 2015;14(9):2394–404.
56. Li P, Fu X, Chen M, Zhang L, Li S. Proteomic profiling and integrated analysis with transcriptomic data bring new insights in the stress responses of Kluyveromyces marxianus after an arrest during high-temperature ethanol fermentation. Biotechnol Biofuels. 2019;12:49.
57. Wen B, Mei Z, Zeng C, Liu S. metaX: a flexible and comprehensive software for processing metabolomics data. BMC Bioinformatics. 2017;18(1):183.
58. Zeng S, Peng O, Hu F, Xia Y, Geng R, Zhao Y, et al. Metabolomic analysis of porcine intestinal epithelial cells during swine acute diarrhea syndrome coronavirus infection. Front Cell Infect Microbiol. 2022;12:1079297.
59. Li R, Li Y, Kristiansen K, Wang J. SOAP: short oligonucleotide alignment program. Bioinformatics. 2008;24(5):713–4.
60. Kim D, Langmead B, Salzberg SL. HISAT: a fast spliced aligner with low memory requirements. Nat Methods. 2015;12(4):357–60.
61. Benelli M, Pescucci C, Marseglia G, Severgnini M, Torricelli F, Magi A. Discovering chimeric transcripts in paired-end RNA-seq data by using EricScript. Bioinformatics. 2012;28(24):3232–9.
62. Shen S, Park JW, Lu ZX, Lin L, Henry MD, Wu YN, et al. rMATS: robust and flexible detection of differential alternative splicing from replicate RNA-Seq data. Proc Natl Acad Sci U S A. 2014;111(51):E5593–601.
63. Langmead B, Salzberg SL. Fast gapped-read alignment with Bowtie 2. Nat Methods. 2012;9(4):357–9.
64. Li B, Dewey CN. RSEM: accurate transcript quantification from RNA-Seq data with or without a reference genome. BMC Bioinformatics. 2011;12:323.
65. Love MI, Huber W, Anders S. Moderated estimation of fold change and dispersion for RNA-seq data with DESeq2. Genome Biol. 2014;15(12):550.
66. Wang L, Feng Z, Wang X, Wang X, Zhang X. DEGseq: an R package for identifying differentially expressed genes from RNA-seq data. Bioinformatics. 2010;26(1):136–8.
67. Audic S, Claverie JM. The significance of digital gene expression profiles. Genome Res. 1997;7(10):986–95.
68. Teixeira V, Martins TS, Prinz WA, Costa V. Target of Rapamycin Complex 1 (TORC1), Protein Kinase A (PKA) and Cytosolic pH Regulate a Transcriptional Circuit for Lipid Droplet Formation. Int J Mol Sci. 2021;22(16):9017.
69. Tamarit J, Irazusta V, Moreno-Cermeno A, Ros J. Colorimetric assay for the quantitation of iron in yeast. Anal Biochem. 2006;351(1):149–51.
70. Monteiro PT, Oliveira J, Pais P, Antunes M, Palma M, Cavalheiro M, et al. YEASTRACT+: a portal for cross-species comparative genomics of transcription regulation in yeasts. Nucleic Acids Res. 2020;48(D1):D642–9.

71. Drapier JC, Hibbs JB Jr. Murine cytotoxic activated macrophages inhibit aconitase in tumor cells Inhibition involves the iron-sulfur prosthetic group and is reversible. J Clin Invest. 1986;78(3):790–7.
72. Strain J, Lorenz CR, Bode J, Garland S, Smolen GA, Ta DT, et al. Suppressors of superoxide dismutase (SOD1) deficiency in Saccharomyces cerevisiae Identification of proteins predicted to mediate iron-sulfur cluster assembly. J Biol Chem. 1998;273(47):31138–44.
73. Teixeira MC, Viana R, Palma M, Oliveira J, Galocha M, Mota MN, et al. YEASTRACT+: a portal for the exploitation of global transcription regulation and metabolic model data in yeast biotechnology and pathogenesis. Nucleic Acids Res. 2023;51(D1):D785–91.
74. Bachhawat N, Ouyang Q, Henry SA. Functional characterization of an inositol-sensitive upstream activation sequence in yeast A cis-regulatory element responsible for inositol-choline mediated regulation of phospholipid biosynthesis. J Biol Chem. 1995;270(42):25087–95.
75. Henry SA, Kohlwein SD, Carman GM. Metabolism and regulation of glycerolipids in the yeast Saccharomyces cerevisiae. Genetics. 2012;190(2):317–49.
76. Henry SA, Patton-Vogt JL. Genetic regulation of phospholipid metabolism: yeast as a model eukaryote. Prog Nucleic Acid Res Mol Biol. 1998;61:133–79.
77. Gaspar ML, Aregullin MA, Chang YF, Jesch SA, Henry SA. Phosphatidic acid species 34:1 mediates expression of the myo-inositol 3-phosphate synthase gene INO1 for lipid synthesis in yeast. J Biol Chem. 2022;298(7):102148.
78. Gaspar ML, Chang YF, Jesch SA, Aregullin M, Henry SA. Interaction between repressor Opi1p and ER membrane protein Scs2p facilitates transit of phosphatidic acid from the ER to mitochondria and is essential for INO1 gene expression in the presence of choline. J Biol Chem. 2017;292(45):18713–28.
79. Han J, Kaufman RJ. The role of ER stress in lipid metabolism and lipotoxicity. J Lipid Res. 2016;57(8):1329–38.
80. Halbleib K, Pesek K, Covino R, Hofbauer HF, Wunnicke D, Hanelt I, et al. Activation of the Unfolded Protein Response by Lipid Bilayer Stress. Mol Cell. 2017;67(4):673-84 e8.
81. Lajoie P, Moir RD, Willis IM, Snapp EL. Kar2p availability defines distinct forms of endoplasmic reticulum stress in living cells. Mol Biol Cell. 2012;23(5):955–64.
82. Merksamer PI, Trusina A, Papa FR. Real-time redox measurements during endoplasmic reticulum stress reveal interlinked protein folding functions. Cell. 2008;135(5):933–47.
83. Promlek T, Ishiwata-Kimata Y, Shido M, Sakuramoto M, Kohno K, Kimata Y. Membrane aberrancy and unfolded proteins activate the endoplasmic reticulum stress sensor Ire1 in different ways. Mol Biol Cell. 2011;22(18):3520–32.
84. Shen H, Heacock PN, Clancey CJ, Dowhan W. The CDS1 gene encoding CDP-diacylglycerol synthase in Saccharomyces cerevisiae is essential for cell growth. J Biol Chem. 1996;271(2):789–95.
85. Wang S, Idrissi FZ, Hermansson M, Grippa A, Ejsing CS, Carvalho P. Seipin and the membrane-shaping protein Pex30 cooperate in organelle budding from the endoplasmic reticulum. Nat Commun. 2018;9(1):2939.
86. Haurie V, Boucherie H, Sagliocco F. The Snf1 protein kinase controls the induction of genes of the iron uptake pathway at the diauxic shift in Saccharomyces cerevisiae. J Biol Chem. 2003;278(46):45391–6.
87. Kaplan J, McVey Ward D, Crisp RJ, Philpott CC. Iron-dependent metabolic remodeling in S. cerevisiae. Biochim Biophys Acta. 2006;1763(7):646–51.
88. Horie T, Kawamata T, Matsunami M, Ohsumi Y. Recycling of iron via autophagy is critical for the transition from glycolytic to respiratory growth. J Biol Chem. 2017;292(20):8533–43.
89. Ueta R, Fujiwara N, Iwai K, Yamaguchi-Iwai Y. Mechanism underlying the iron-dependent nuclear export of the iron-responsive transcription factor Aft1p in Saccharomyces cerevisiae. Mol Biol Cell. 2007;18(8):2980–90.
90. de Nadal E, Posas F. The HOG pathway and the regulation of osmoadaptive responses in yeast. FEMS Yeast Res. 2022:foac013.
91. Proft M, Serrano R. Repressors and upstream repressing sequences of the stress-regulated ENA1 gene in Saccharomyces cerevisiae: bZIP protein Sko1p confers HOG-dependent osmotic regulation. Mol Cell Biol. 1999;19(1):537–46.
92. Pascual-Ahuir A, Posas F, Serrano R, Proft M. Multiple levels of control regulate the yeast cAMP-response element-binding protein repressor Sko1p in response to stress. J Biol Chem. 2001;276(40):37373–8.
93. Proft M, Pascual-Ahuir A, de Nadal E, Arino J, Serrano R, Posas F. Regulation of the Sko1 transcriptional repressor by the Hog1 MAP kinase in response to osmotic stress. EMBO J. 2001;20(5):1123–33.
94. Yamaguchi-Iwai Y, Dancis A, Klausner RD. AFT1: a mediator of iron regulated transcriptional control in Saccharomyces cerevisiae. EMBO J. 1995;14(6):1231–9.
95. Yamaguchi-Iwai Y, Stearman R, Dancis A, Klausner RD. Iron-regulated DNA binding by the AFT1 protein controls the iron regulon in yeast. EMBO J. 1996;15(13):3377–84.
96. Smith A, Ward MP, Garrett S. Yeast PKA represses Msn2p/Msn4p-dependent gene expression to regulate growth, stress response and glycogen accumulation. EMBO J. 1998;17(13):3556–64.
97. Martinez-Pastor MT, Marchler G, Schuller C, Marchler-Bauer A, Ruis H, Estruch F. The Saccharomyces cerevisiae zinc finger proteins Msn2p and Msn4p are required for transcriptional induction through the stress response element (STRE). EMBO J. 1996;15(9):2227–35.
98. Sadeh A, Movshovich N, Volokh M, Gheber L, Aharoni A. Fine-tuning of the Msn2/4-mediated yeast stress responses as revealed by systematic deletion of Msn2/4 partners. Mol Biol Cell. 2011;22(17):3127–38.
99. Muhlhofer M, Offensperger F, Reschke S, Wallmann G, Csaba G, Berchtold E, et al. Deletion of the transcription factors Hsf1, Msn2 and Msn4 in yeast uncovers transcriptional reprogramming in response to proteotoxic stress. FEBS Lett. 2024;598(6):635–57.
100. Diehn M, Alizadeh AA, Rando OJ, Liu CL, Stankunas K, Botstein D, et al. Genomic expression programs and the integration of the CD28 costimulatory signal in T cell activation. Proc Natl Acad Sci U S A. 2002;99(18):11796–801.
101. Stewart-Ornstein J, Nelson C, DeRisi J, Weissman JS, El-Samad H. Msn2 coordinates a stoichiometric gene expression program. Curr Biol. 2013;23(23):2336–45.
102. Kupchak BR, Garitaonandia I, Villa NY, Mullen MB, Weaver MG, Regalla LM, et al. Probing the mechanism of FET3 repression by Izh2p overexpression. Biochim Biophys Acta. 2007;1773(7):1124–32.
103. Stanhill A, Schick N, Engelberg D. The yeast ras/cyclic AMP pathway induces invasive growth by suppressing the cellular stress response. Mol Cell Biol. 1999;19(11):7529–38.
104. SantaMaria AM, Rouault TA. Regulatory and Sensing Iron-Sulfur Clusters: New Insights and Unanswered Questions. Inorganics. 2024;12(4):101.
105. Chen OS, Crisp RJ, Valachovic M, Bard M, Winge DR, Kaplan J. Transcription of the yeast iron regulon does not respond directly to iron but rather to iron-sulfur cluster biosynthesis. J Biol Chem. 2004;279(28):29513–8.
106. Dowhan W. Role of phospholipids in Escherichia coli cell function. In: Tartakoff AM, Dalbey RE, editors. Advances in Cellular and Molecular Biology of Membranes and Organelles. 1995;4:189–217.
107. Wolinski H, Hofbauer HF, Hellauer K, Cristobal-Sarramian A, Kolb D, Radulovic M, et al. Seipin is involved in the regulation of phosphatidic acid metabolism at a subdomain of the nuclear envelope in yeast. Biochim Biophys Acta. 2015;1851(11):1450–64.
108. Han S, Binns DD, Chang YF, Goodman JM. Dissecting seipin function: the localized accumulation of phosphatidic acid at ER/LD junctions in the absence of seipin is suppressed by Sei1p(DeltaNterm) only in combination with Ldb16p. BMC Cell Biol. 2015;16:29.
109. Wang CW, Miao YH, Chang YS. Control of lipid droplet size in budding yeast requires the collaboration between Fld1 and Ldb16. J Cell Sci. 2014;127(Pt 6):1214–28.
110. Hancock LC, Behta RP, Lopes JM. Genomic analysis of the Opi- phenotype. Genetics. 2006;173(2):621–34.
111. Masuda M, Miyazaki-Anzai S, Keenan AL, Okamura K, Kendrick J, Chonchol M, et al. Saturated phosphatidic acids mediate saturated fatty acid-induced vascular calcification and lipotoxicity. J Clin Invest. 2015;125(12):4544–58.
112. Perez-Marti A, Ramakrishnan S, Li J, Dugourd A, Molenaar MR, De La Motte LR, et al. Reducing lipid bilayer stress by monounsaturated fatty acids protects renal proximal tubules in diabetes. Elife. 2022;11:e74391.
113. Ahmad S, Orellana A, Kohler I, Frolich L, de Rojas I, Gil S, et al. Association of lysophosphatidic acids with cerebrospinal fluid biomarkers and progression to Alzheimer's disease. Alzheimers Res Ther. 2020;12(1):124.

114. Yang XY, Zhao EY, Zhuang WX, Sun FX, Han HI, Han HR, et al. LPA signaling is required for dopaminergic neuron development and is reduced through low expression of the LPA1 receptor in a 6-OHDA lesion model of Parkinson's disease. Neurol Sci. 2015;36(11):2027–33.
115. Dedoni S, Camoglio C, Siddi C, Scherma M, Fratta W, Fadda P. The Role of Lysophosphatidic Acid in Neuropsychiatric and Neurodegenerative Disorders. Future Pharmacol. 2024;4(1):199–221.
116. Ou Z, Sun Y, Lin L, You N, Liu X, Li H, et al. Olig2-Targeted G-Protein-Coupled Receptor Gpr17 Regulates Oligodendrocyte Survival in Response to Lysolecithin-Induced Demyelination. J Neurosci. 2016;36(41):10560–73.
117. Qiao J, Huang F, Naikawadi RP, Kim KS, Said T, Lum H. Lysophosphatidylcholine impairs endothelial barrier function through the G protein-coupled receptor GPR4. Am J Physiol Lung Cell Mol Physiol. 2006;291(1):L91-101.
118. Muramatsu R, Kuroda M, Matoba K, Lin H, Takahashi C, Koyama Y, Yamashita T. Prostacyclin prevents pericyte loss and demyelination induced by lysophosphatidylcholine in the central nervous system. J Biol Chem. 2015;290(18):11515–25.
119. Sheikh AM, Michikawa M, Kim SU, Nagai A. Lysophosphatidylcholine increases the neurotoxicity of Alzheimer's amyloid beta1-42 peptide: role of oligomer formation. Neuroscience. 2015;292:159–69.
120. Kaya I, Brinet D, Michno W, Baskurt M, Zetterberg H, Blenow K, Hanrieder J. Novel Trimodal MALDI Imaging Mass Spectrometry (IMS3) at 10 mum Reveals Spatial Lipid and Peptide Correlates Implicated in Abeta Plaque Pathology in Alzheimer's Disease. ACS Chem Neurosci. 2017;8(12):2778–90.
121. Tzekov R, Dawson C, Orlando M, Mouzon B, Reed J, Evans J, et al. Sub-chronic neuropathological and biochemical changes in mouse visual system after repetitive mild traumatic brain injury. PLoS ONE. 2016;11(4):e0153608.
122. Gupta M, Outten CE. Iron-sulfur cluster signaling: The common thread in fungal iron regulation. Curr Opin Chem Biol. 2020;55:189–201.
123. Rutherford JC, Ojeda L, Balk J, Muhlenhoff U, Lill R, Winge DR. Activation of the iron regulon by the yeast Aft1/Aft2 transcription factors depends on mitochondrial but not cytosolic iron-sulfur protein biogenesis. J Biol Chem. 2005;280(11):10135–40.
124. Zhu J, Xu F, Lai H, Yuan H, Li XY, Hu J, et al. ACO2 deficiency increases vulnerability to Parkinson's disease via dysregulating mitochondrial function and histone acetylation-mediated transcription of autophagy genes. Commun Biol. 2023;6(1):1201.
125. Lepore E, Lauretta R, Bianchini M, Mormando M, Di Lorenzo C, Unfer V. Inositols Depletion and Resistance: Principal Mechanisms and Therapeutic Strategies. Int J Mol Sci. 2021;22(13):6796.
126. Anwar S, Alrumaihi F, Sarwar T, Babiker AY, Khan AA, Prabhu SV, Rahmani AH. Exploring Therapeutic Potential of Catalase: Strategies in Disease Prevention and Management. Biomolecules. 2024;14(6):697.
127. Zhou ZD, Tan EK. Iron regulatory protein (IRP)-iron responsive element (IRE) signaling pathway in human neurodegenerative diseases. Mol Neurodegener. 2017;12(1):75.

Publisher's Note